LA-UR-22-24095
Accepted Manuscript

Estimating snow cover from high-resolution satellite imagery by thresholding blue wavelengths

Thaler, Evan Austin
Crumley, Ryan Landon
Bennett, Katrina Eleanor

To be published in: Remote Sensing of Environment

DOI to publisher's version: 10.1016/j.rse.2022.113403

Permalink to record:
http://permalink.lanl.gov/object/view?what=info:lanl-repo/lareport/LA-UR-22-24095

Estimating snow cover from high-resolution satellite imagery by thresholding blue wavelengths

Evan A. Thaler[1], Ryan L. Crumley[1], Katrina E. Bennett[1]

[1]Earth and Environmental Sciences Division, Los Alamos National Laboratory. Los Alamos, NM, USA

Abstract

The extent and duration of snow cover, a critical component of the hydrologic cycle and the global climate system, is expected to shift dramatically under climate change. Therefore, developing high-resolution assessments of snow cover change is crucial for estimating the impact of changing snow cover on the hydrologic system, as well as for understanding other fundamental processes, such as snow-vegetation and snow-permafrost feedbacks. Remote sensing tools provide a powerful method for mapping snow-covered area (SCA) across a landscape. The most common method for estimating SCA utilizes the normalized difference snow index (NDSI), which relies on spectral measurements in the shortwave-infrared wavelengths (SWIR). NDSI can effectively estimate catchment- to regional-scale SCA, but it cannot be used to assess fine-scale SCA because of current limitations on the resolution of satellite-derived SWIR measurements. Here, we map SCA using only a threshold of blue wavelengths and high-resolution satellite imagery. The thresholding method, which we call the Blue Snow Threshold algorithm (BST), has previously been used with digital camera imagery, but here we refine and automate the algorithm for use with cloud-free high-resolution satellite imagery and find that the BST can be used to assess fine-scale SCA when clouds are not present. For validation, we compared BST-derived estimates of SCA to a) airborne lidar surveys, b) Landsat fractional SCA, and c) snow disappearance dates from Snow Telemetry (SNOTEL) stations. When compared to airborne lidar surveys of SCA, the BST predicted SCA had a range of F-scores between 0.81 and 0.94 in four study areas in California and Colorado. We also found general agreement between SCA and snow disappearance at multiple SNOTEL sites across the western United States. Given the relatively recent availability of high-resolution satellite imagery with spectral measurements in the visible wavelengths but lacking in SWIR, the BST offers a reliable and easy-to-apply tool for examining fine-scale snow-related processes.

1. Introduction

Snow is integral to the global climate system because its high albedo reflects incoming solar radiation, regulating the amount of solar energy transferred to the land surface, especially during the spring months in the Northern Hemisphere (Budyko, 1969; Déry and Brown, 2007; Groisman et al., 1994; Sellers, 1969; Thackeray and Fletcher, 2016). Due to its low thermal conductivity, snow also insulates the underlying ground from atmospheric influences, which can lead to higher soil temperatures beneath the snow (Barry, 1996; Zhang, 2005). In high-latitude and high-altitude hydrologic systems, snow is a dominant source of groundwater recharge and river discharge (Adam et al., 2009; Callaghan et al., 2011; Liston and Hiemstra, 2011; Mote et al., 2005; Stewart et al., 2005). As high-latitude and high-altitude regions of the planet warm and seasonal precipitation patterns shift under climate change, high spatial and temporal resolution maps of snow cover are critical for evaluating impacts to both regional hydrology and local-scale changes in snowpack duration and extent.

Understanding the extent and duration of snow cover is integral to many ecosystem and geologic processes in cold regions. Permafrost soils are particularly sensitive to the insulating effects of seasonal snow depth because permafrost thaw and degradation is amplified in areas with long-duration snow cover (Biskaborn et al., 2019; Gisnås et al., 2014; Park et al., 2015; Smith et al., 2022; Uhlemann et al., 2021; Zhang et al., 1997). Likewise, Arctic tundra plant communities, species composition, and phenology are heavily dependent on the quantity of winter snow and the timing of snow melt (Kelsey et al., 2021; Mekonnen et al., 2021; Niittynen et al., 2020; Schmidt et al., 2019; Wilcox et al., 2019). Field campaigns which aim to capture the timing of snowmelt and map snow-covered area (SCA) are spatially and temporally limited, particularly in remote regions like the Arctic (Bennett et al., 2021). Hence, field observations alone are unable to evaluate regional changes in snow cover extent and duration.

Remote sensing has proven to be a powerful method for mapping SCA at regional scales (Bennett et al., 2019; Crumley et al., 2020; Dietz et al., 2012; Hall et al., 2002; Nolin, 2010; Rittger et al., 2013). Of all natural materials, snow has among the highest reflectance of radiation in the visible wavelengths (Figure 1; Meerdink et al., 2019; Nolin, 2010), and the reflectance can even be greater than that of clouds (e.g., Figure 2 in Dong, 2018).The high reflectance of snow is a unique property which has made optical remote sensing methods of snow mapping attainable. Scientists have a long history of using visible wavelengths to estimate SCA. From the 1960s through the early 1990s, the National Oceanic and Atmospheric Administration (NOAA) employed trained meteorologists to analyze true-color, visible satellite images of snow cover extent in the northern hemisphere in order to create weekly maps of SCA (Matson and Wiesnet, 1981; Wiesnet et al., 1987). These maps were derived from multiple satellite platforms, like the early Very High Resolution Radiometer (VHRR), the Advanced Very High Resolution Radiometer (AVHRR), the Geostationary Operational Environmental

Satellite (GOES), and MeteoSat (Groisman et al., 1994). The NOAA snow cover maps served as the basis for decision making about the timing and spatial extent of spring snowmelt and as a climate record in long-term studies of weather and climate, even though they were relatively low-resolution and manually drawn (Groisman et al., 1994; Robinson et al., 1993).

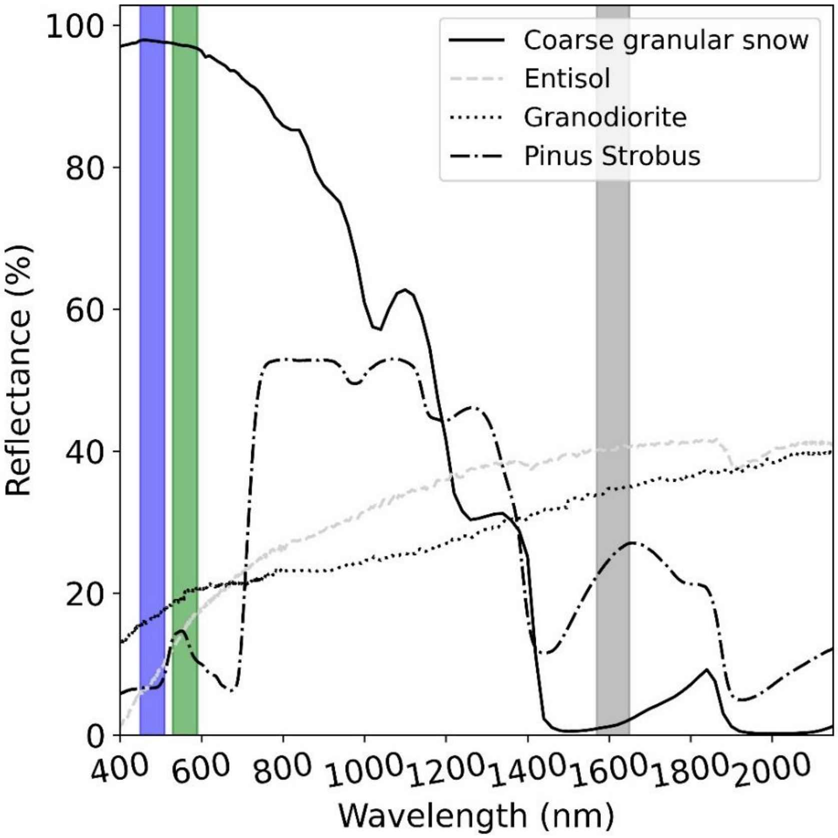

Figure 1. Examples of spectral curves for common natural materials. The blue, green, and gray shaded area indicate the blue, green, and shortwave infrared wavelengths, respectively. Within the blue wavelengths, coarse granular snow has a nearly 80% greater reflectance than the other natural objects. Spectral data are from the Ecostress Spectral Library (Meerdink et al., 2019).

The Normalized Difference Snow Index (NDSI; Dozier, 1989; Rango and Itten, 1976) has become the most commonly used optical remote sensing index for identifying snow-covered land surfaces. NDSI is defined as:

$$NDSI = \frac{(\rho_{green} - \rho_{swir})}{(\rho_{green} + \rho_{swir})} \qquad (1)$$

where ρ_{green} and ρ_{swir} are spectral reflectance (ρ) in the green and shortwave infrared (SWIR) wavelengths, respectively. NDSI leverages the high ρ_{green} and low ρ_{swir} of snow (Figure 1), and binary classifications for the presence or absence of snow typically use a threshold of NDSI >0.4, where pixels with NDSI values greater than the threshold are classified as snow.

Whereas the binary classification of SCA using NDSI provides a prediction of the presence or absence of snow cover, fractional SCA (fSCA) algorithms estimate the fraction of a given pixel estimated to contain snow (Gascoin et al., 2020; Painter et al., 2009; Rittger et al., 2013; Salomonson and Appel, 2004; Selkowitz and Forster, 2016). Some studies use a multivariate polynomial regression approach to derive fSCA from NDSI (Barton et al., 2000; Salomonson and Appel, 2004), while others employ multiple endmember spectral analysis approaches (Nolin et al., 1993; Painter et al., 2009). The primary SCA products are the MOD10A1 Modis/Terra Snow Cover grid (Hall and Riggs, 2021; Hall et al., 2002), the Modis Snow Cover Area and Grain Size (MODSCAG) product (Painter et al., 2009; Rittger et al., 2013), and the Landsat fSCA (Selkowitz et al., 2015.; Selkowitz and Forster, 2016). Landsat fSCA is a 30 m spatial resolution data product generated from Landsat Collection 1 surface reflectance and top of atmosphere reflectance data from imagery acquired by Landsat 4-8. The MOD10A1 and MODSCAG products both estimate SCA at 500 m. Although these snow cover products are effective at mapping fSCA at regional and basin scales (e.g., Salomonson and Appel, 2004), satellite remote sensing-derived estimates of SCA at the sub-hillslope scale are lacking.

While Landsat and MODI10A1 products are widely used, they do have limitations. The frequency of Landsat image acquisition every 16 days limits the use of the Landsat fSCA product for studies that require high temporal frequency. And although the MODIS SCA are daily products, the 500 m spatial resolution of the product is too coarse for hillslope-scale resolution, which is necessary to evaluate important snow feedback processes, such as the influence of snow cover on permafrost degradation or the heterogeneity of snow disappearance in complex topography (Parr et al., 2020). Therefore, to map SCA at the sub-hillslope scale, we need datasets with high spatial resolution and high temporal frequency, along with a method to predict SCA that does not rely on SWIR wavelengths.

Non-optical remote sensing methods such as airborne laser scanning (ALS; e.g., Kostadinov et al., 2019; Painter et al., 2016) and synthetic aperture radar (SAR; e.g., Nagler et al., 2016) have been developed to generate SCA and snow depth measurements in areas where optical sensors traditionally perform poorly. For example, ALS is particularly useful for generating high spatial resolution estimates of snowpack properties below the canopy in densely forested ecosystems (Kostadinov et al., 2019) where imaging from optical sensors is severely limited (Muhuri et al., 2021). SAR-based approaches to estimating snow properties have been explored to overcome the limitations of optical sensors, such as cloud cover and darkness, which are especially detrimental to optical estimates of winter snow properties in high-latitude regions (Tsai et al., 2019). Although both ALS and SAR are effective at mapping snow distributions, the widespread application of ALS, which can produce very high-resolution estimates, is limited by the necessity of airborne missions that cover a small footprint and are costly. SAR data suffer from the need for expert processing and interpretation (Lillesand et al., 2015) and a resultant resolution (5 x 20m for Sentinel-2) that is too coarse for evaluating hillslope-scale processes driven by snow accumulation and redistribution.

Commercial satellite imagery provides a means by which SCA can be estimated at high spatial resolution and high temporal frequency. Multispectral reflectance is measured at high resolution (≤5 m) by commercial satellites, which provide free imagery for U.S. government researchers (Neigh et al., 2013). For example, the PlanetScope satellite constellation from Planet Labs (Planet Labs Inc., 2019) has been increasing global image acquisition frequency to near daily resolution over the past decade, with imagery products ranging in spatial resolution from 3 to 5 m. However, commercial satellites have only limited measurements of reflectance in the SWIR wavelengths (Planet, for example, does not measure SWIR), which prohibits the widespread use of these satellite products for NDSI calculation. Yet, despite these spectral limitations, the suitability of commercial satellite imagery for estimating SCA has recently been demonstrated (Cannistra et al., 2021; Hu and Shean, 2022; John et al., 2022) . Using a machine learning approach that incorporated 3 m, 4-band PlanetScope imagery, SCA was, on average, accurately predicted for 73% of pixels in a forested basin in California and 62% of pixels in a climatologically different basin in Colorado (Cannistra et al., 2021). While these results are encouraging, ease and accessibility of estimating SCA from commercial imagery could be facilitated by the development of a method that solely leverages the high visible wavelength reflectance of snow and does not rely on advanced statistical techniques.

A previously developed, simple method for binary assessment of SCA leverages the high spectral reflectance of snow in the visible spectrum by using a thresholding method based on a typically bimodal distribution of ρ_{blue} (Fedorov et al., 2016; Salvatori et al., 2011). Although simplistic, the thresholding method has been shown to be effective in generating binary predictions of SCA from oblique digital camera and webcam images (Aalstad et al., 2020; Salvatori et al., 2011; Salzano et al., 2019), but to our knowledge, has not been used to derive SCA from high-resolution satellite imagery. Because the thresholding method relies only on the ρ_{blue} of an image, it can be applied to cloud-free, high-resolution true-color imagery, such as that acquired by commercial satellites.

Here, we develop an automated algorithm, which we call the Blue Snow Threshold algorithm (BST), that, for a given satellite image, dynamically defines a threshold ρ_{blue}, which is used to generate a binary classification of snow versus non-snow pixels. We then apply the BST to high spatiotemporal resolution satellite imagery to generate binary SCA predictions. First, we compare BST-derived SCA to snow cover maps generated from airborne lidar surveys at two sites in California and two in Colorado. Next, we compare BST-derived SCA to estimates derived from Landsat fSCA at five sites across the western U.S., including three sites in Alaska. Then, we compare the snow disappearance date determined from snow depth measurements at four snow telemetry stations to the snow disappearance date estimated by BST-derived SCA for the same locations. Finally, we discuss the suitability of commercial satellite imagery acquired at high spatial resolution and high temporal frequency for estimating fine-scale spatial and temporal changes in SCA across our study sites.

2. Data & Methods

2.1 Binary snow masks generated from the BST

Generating binary masks of SCA from multispectral imagery requires the use of a threshold on specific bands or indices. For example, a pixel is considered snow-covered when NDSI > 0.40, ρ_{NIR} >0.11, and ρ_{green} >0.10 (Nolin, 2010). Similarly, the BST calculates a threshold value to generate binary snow mask classifications; however, unlike the fixed NDSI thresholds, the BST algorithm dynamically defines a threshold ρ_{blue} value for a given image based on first, the $\overline{\rho_{blue}}$ and second, the smoothed histogram of ρ_{blue} for the image.

Each pixel in the satellite image is classified as either snow-covered (1) or non-snow (0) according to the following condition:

$$S(x,y) = \begin{cases} 1 & \rho_{blue}(x,y) \geq t \\ 0 & else \end{cases} \quad (2)$$

where $S(x,y)$ *is* a pixel within a given image which is being classified, $\rho_{blue}(x,y)$ is the ρ_{blue} for the pixel, and *t* is the threshold defining snow versus non-snow pixels for the entire image. The determination of *t* is described in detail below and is visually demonstrated as a flow chart in Figure 2.

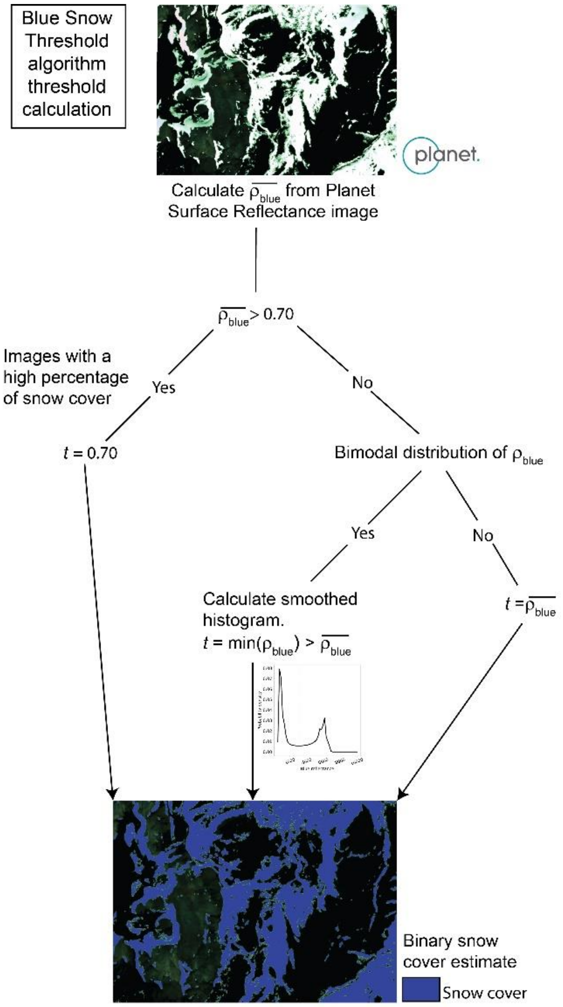

Figure 2. Flow chart demonstrating the automated threshold (*t*) calculation procedure of the Blue Snow Threshold algorithm. Images with a high percentage of snow cover follow the left side of the chart, and images with mixed snow and non-snow pixels follow the right side of the chart.

2.1.1 Threshold for images containing a high snow cover percentage

In the case when an image is nearly or fully snow-covered (e.g., Figure 3a), the distribution of ρ_{blue} has a negative skew (Figure 3b; Salvatori et al., 2011; Aalstad et al., 2020). Because of the high ρ_{blue} of snow (Figure 1), images dominated by snow-cover have a $\overline{\rho_{blue}}$ > 0.70 (or 7,000 for PlanetScope images, which are scaled by 10,000) (Figure 3b; Salvatori et al., 2011), whereas images with a comparable mixture of snow and non-snow pixels, $\overline{\rho_{blue}}$ is << 0.7 (Figure 3d,e). Therefore, the first procedure in the BST algorithm is the calculation of $\overline{\rho_{blue}}$. When $\overline{\rho_{blue}}$ > 0.70, the BST algorithm assumes that the image is composed primarily of snow pixels (Figure 3a) and uses a fixed *t* = 0.70 (Figures 2,3b), above which all values are classified as snow (Figure 3c).

The threshold value of 0.70 was chosen because it is nearly double the $\overline{\rho_{blue}}$ for mixed snow and non-snow images (see Figure 3b,e).

2.1.2 Threshold for mixed snow and non-snow images.

For images where $\overline{\rho_{blue}} < 0.70$, the BST assumes the image is only partially snow-covered and calculates the smoothed histogram of ρ_{blue}. Images with partial snow cover (Figure 3d) often have a bimodal distribution of ρ_{blue} (Figure 3e; Salvatori et al., 2011; Fedorov et al., 2016; Aalstad et al., 2020). The dynamic threshold approach takes advantage of this bimodality. The algorithm tests for bimodality using Hartigan's dip test for unimodality (Hartigan, 1985) implemented using the *diptest* package in *Python*. When ρ_{blue} is bimodally distributed, *t* is defined as the first local minimum where $\rho_{blue} > \overline{\rho_{blue}}$ (Figures 2,3e). In most cases, *t* for a partially snow-covered image with a bimodal distribution of ρ_{blue} is found in the trough between the peaks although it is not necessarily the minimum ρ_{blue} within the trough (Figure 3e). For cases where the distribution is monomodal, $t = \overline{\rho_{blue}}$ (Figure 2). In the case where the ρ_{blue} distribution is monomodal with zero skew, *t* will be the peak of the distribution. Note that this case never occurs in our images. In cases of positive skewness, which occurs often (supplementary Figure S1), *t* will be greater than the peak.

We note that an image with nearly full snow coverage (Figure 3a) can also have a bimodal distribution of ρ_{blue} (Figure 3b). However, the ρ_{blue} values are negatively skewed with the peaks of the distribution occurring at > 0.70. For example, Figure 3a has ρ_{blue} peaks at 0.8 (8,000) and 0.9 (9,000) (Figure 3b). If the threshold for the image was determined using the thresholding procedure based on the bimodality of the histogram, as described in this subsection (2.1.2), the algorithm would generate a snow mask which significantly underestimates the true snow cover. For this image, the algorithm would choose the first local minimum $\rho_{blue} > \overline{\rho_{blue}}$, which is > 0.86. Hence, for images which have a high percentage of snow, we use a fixed threshold of 0.70 to incorporate pixels with greater ρ_{blue} values that are indicative of snow. We include more examples of threshold selection for snow-covered imagery in the supplementary materials in Figure S2.

2.1.3 Application to high-resolution satellite imagery

For the analysis in this study, we applied the BST to high spatiotemporal satellite imagery available from Planet Labs, Inc. (Planet; Planet Labs Inc., 2019). Planet imagery is acquired from a constellation of CubeSats (PlanetScope), which are small satellites (10 cm by 10 cm by 30 cm) equipped with optical sensors. The PlanetScope constellation comprises nearly 130 satellites operating in sun-synchronous orbit and collecting daily images of the global land surface. We use the cloud-free Level-3B multispectral “Analytic Surface Reflectance” (SR) images, which are orthorectified and available as 16-bit, 3-5 m resolution products with spectral data in the visible and near infrared wavelengths (Marta, 2018). The reflectance values in the SR images are scaled by 10,000 to avoid quantization errors (Frazier and Hemingway, 2021; Marta, 2018), resulting in a final SR product that is not scaled from 0-1, as is typical with other SR products. Each image was determined cloud-free by Planet algorithms. However, the cloud mask offered by Planet has been demonstrated to misclassify snow as clouds (Cannistra et al., 2021); therefore, we manually inspected each image for the presence of clouds and conservatively excluded portions of the image which appeared to contain clouds.

PlanetScope images contain several tens of thousands of pixels, which results in a noisy distribution of ρ_{blue}, and calculating the threshold on imagery first requires smoothing the ρ_{blue} distribution, so that the true interpeak minimum can be determined. We smoothed the arrays using a 1-d gaussian filter implemented in *Python* (*scipy.ndimage.gaussian_filter1d*) with a smoothing width of 3, which was iteratively chosen from a range of 1-50 as the value which minimized noise in the data but retained the overall peaks and troughs of the distribution. An example of the threshold selection procedure is demonstrated in Figures 2 and 3.

To estimate SCA in this study, we used the “Surface Reflectance” imagery product which is recommended by Planet for analysis applications. We also performed SCA analysis with the atmospherically uncorrected RGB product (called “Visual” by Planet) to assess the need for atmospheric correction of satellite imagery prior to applying the BST. We find that when applying the BST procedure to the atmospherically uncorrected imagery, the algorithm overestimates the snow extent. More details about this comparison are given in the Supplementary Material.

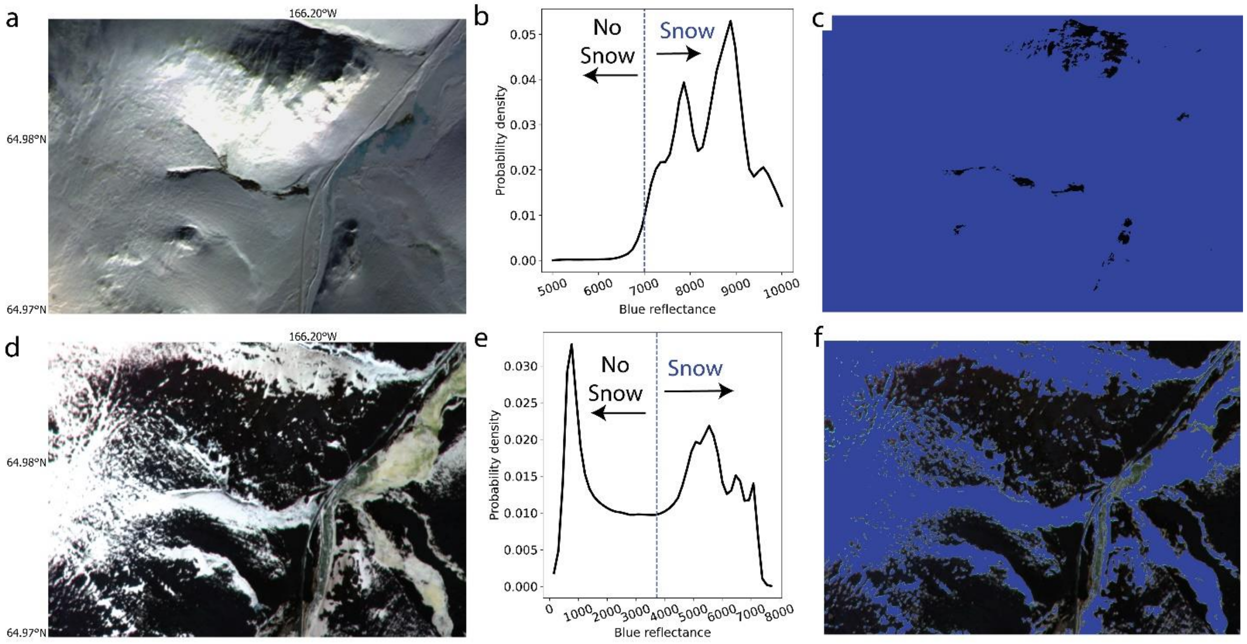

Figure 3. Example of the threshold selection for binary classification of pixels using the Blue Snow Threshold algorithm (BST). The image is a 16-bit surface reflectance product, which is scaled by a factor of 10,000. a) Example of threshold selection for an image primarily composed of snow-covered pixels. PlanetScope true-color satellite image of a location on the Seward Peninsula (see Figure 5a) acquired on March 04, 2020. b) Distribution of ρ_{blue} values from the snow-covered image. In this image $\overline{\rho_{blue}}$ is 0.86 (8,600), which is > $\overline{\rho_{blue}}$ defined by the algorithm for mixed snow non-snow images (0.70); therefore, *t* is set to the fixed value of 0.70 (7,000) c) Snow mask generated from the BST. Blue pixels indicate those classified as snow. d) PlanetScope true-color satellite image of a location on the Seward Peninsula (see Figure 5a) acquired on May 05, 2020. e) Smoothed distribution of ρ_{blue} values from the image with the threshold shown as the blue dashed line. The threshold (*t*) in this example is 0.37 (3,700). Values greater than the threshold are considered snow, whereas values less than the threshold are non-snow pixels. f) Snow mask generated from the BST. Blue areas indicate pixels classified as snow.

2.2 Comparison of the BST to airborne lidar surveys

We used four watersheds across the western United States to validate the BST-derived SCA against SCA derived from ALS. These locations in California and Colorado are within the network of watersheds measured by the Airborne Snow Observatory (ASO) as sites to generate snow depth measurements derived from a coupled imagining spectrometer and lidar scanner and repeat scans of a given area (Painter et al., 2016,https://www.airbornesnowobservatories.com). The ASO generates snow depth rasters at 3 m spatial resolution at repeated intervals from March-June for several watersheds across the western United States.

For this analysis, we chose ASO sites located within the Yuba River watershed (ASO_Yuba_Mosaic_2022Mar25) and the Tuolumne River watershed (ASO_3M_SD_USCATE_20180528) in California (Figure 4a), and the Conejos River watershed (ASO_Conejos_Mosaic_2021Apr20-21) and the Blue River watershed (ASO_BlueRiver_2021Apr18) in Colorado (Figure 4b). The Tuolumne River watershed ASO site is one of the same study sites used by Cannistra et al. (2021). For each ASO site, we used the National Land Cover Database (Homer et al., 2007) to assess the dominant vegetation types (Table 1). Vegetation at the four ASO sites is a mixture of grassland, shrubs, evergreen and deciduous forests (Table 1). For ASO each site, except for Tuolumne, for which some data are unavailable, April 1st snow water equivalent (SWE), annual precipitation, and winter (calculated as December-January-February, DJF) temperatures were calculated (Table 2**).**

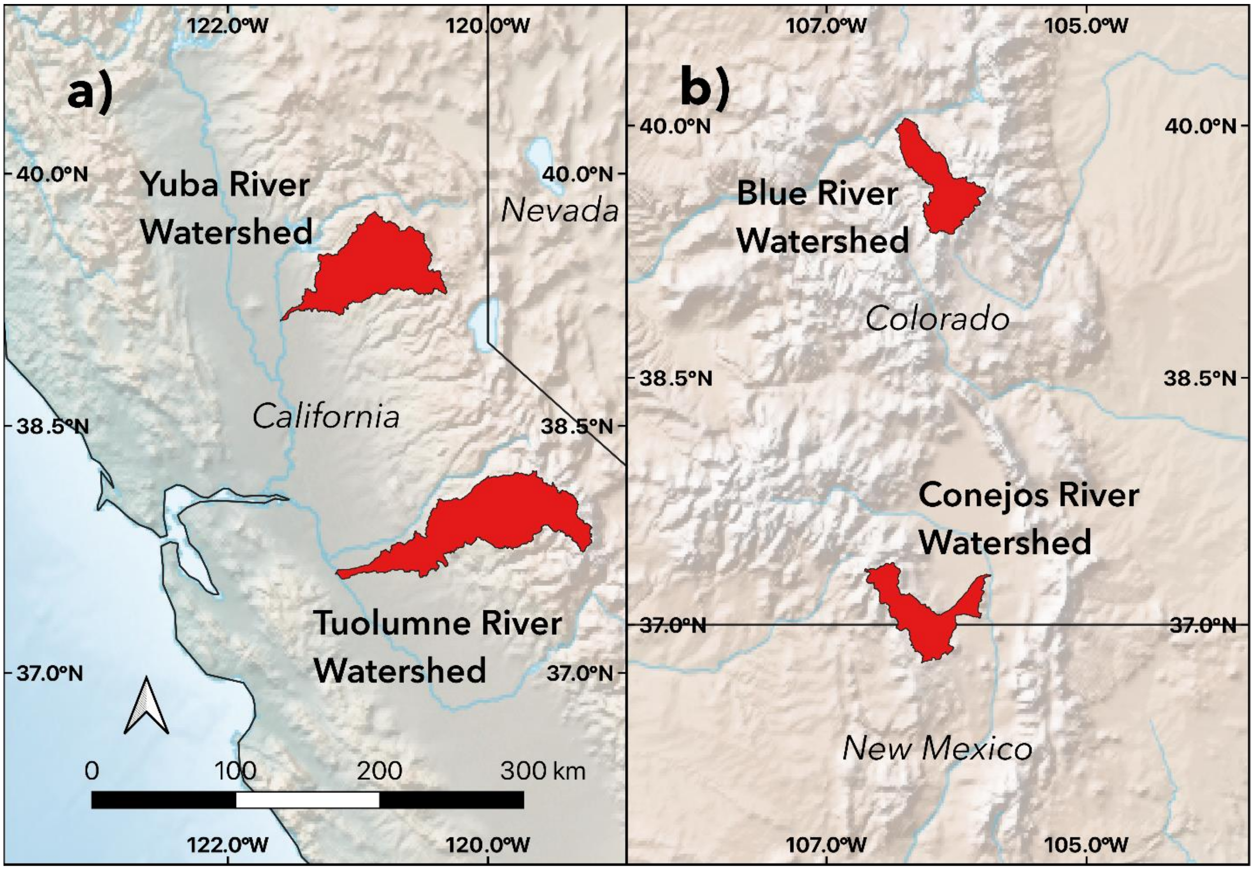

Figure 4. Airborne lidar surveys map: **(a)** the Yuba River and Tuolumne River watersheds in California, and **(b)** the Blue River and Conejos River watersheds in

Colorado where the Airborne Snow Observatory acquired lidar datasets of snow depth for multiple years.

For each site, we used PlanetScope imagery collected contemporaneously with the ASO surveys to ensure snow conditions in the image were representative of conditions during the lidar surveys. We validated BST-derived SCA against snow masks generated from airborne lidar surveys of snow depth (3 m spatial resolution) collected at the ASO. To evaluate the accuracy of BST-derived SCA predictions, we consider the ASO datasets as the “ground truth.” Binary snow cover masks were generated from the ASO datasets by using a threshold snow depth of 0.1 m, such that only pixels with a snow depth ≥ 0.1 m were classified as snow. The threshold value is consistent with prior thresholding used to generate binary snow cover rasters from ASO data products (Cannistra et al., 2021).

For each ASO site, the BST was applied to PlanetScope imagery acquired within one day of the ASO retrieval. At the Tuolumne ASO site, we used the 2018 lidar acquisition and applied the BST to the same PlanetScope images used in Cannistra et al., (2021) to directly compare the utility of BST to published estimates of SCA derived from a ML model (Cannistra et al., 2021; Painter et al., 2016).

For the statistical comparison at each site, we computed performance metrics of the BST-derived SCA estimates with respect to the ASO snow mask. Specifically, we compute precision, recall, F-score, and balanced accuracy to be consistent with metrics used for predictions at these sites by Cannistra et al., 2021. Precision is the ability of the algorithm to identify only the relevant snow pixels. It is defined as the number of true positives (or pixels identified as snow as identified by the ASO mask) divided by the total number of pixels predicted to be snow by the BST (true positives and false positives).

$$Precision = \frac{True\ Positives}{True\ Positives + False\ Positives} \qquad (2)$$

Recall is a measure of the algorithm’s ability to correctly identify all snow pixels. Recall is defined as the number of pixels identified as snow by the BST divided by the total number of true snow pixels identified by the ASO mask, which includes pixels indicated as no snow by the BST (false negatives).

$$Recall = \frac{True\ Positives}{True\ Positives + False\ Negative} \qquad (3)$$

F-score is the harmonic mean of precision and recall and is the measure of the accuracy of the binary classification with a range of 0 to 1, where values of 1 indicate a perfect classification.

$$Fscore = 2\frac{Precision \cdot Recall}{Precsion + Recall} \quad (4)$$

Balanced accuracy is a normalized ratio between the true positive and true negative predictions from the BST and the true positive and true negative ASO classifications. Balanced accuracy is a particularly useful measure of classification performance when the classes are imbalanced, as is the case for the snow, no-snow classes. For a binary classification, balanced accuracy is calculated as:

$$Balanced\ Accuracy = \frac{True\ Positive\ Rate + True\ Negative\ Rate}{2} \quad (5)$$

2.3 Comparison of the BST to snow telemetry and high-latitude sites

Five additional study locations were chosen to span a range of topographic relief and dominant vegetation type (Figure 5). Four of the study locations are co-located with SNOw TELemetry (SNOTEL) stations (Dressler et al., 2006; Serreze et al., 1999): Quemazon (708) near Los Alamos, NM, Truckee (834) near Truckee, CA, Mt. Ryan (948) near Fairbanks, AK; and Bettles Field (1182) in the southern Brooks Range in AK. The fifth site is located on the Seward Peninsula near Dahl, AK.

The sites span a range of land cover and climatic types. We also calculated April 1st SWE, annual precipitation, and DJF temperatures at each SNOTEL site (Table 2). The average annual precipitation and winter temperatures are notably lower in the sub-Arctic and Arctic sites in Alaska. Truckee has the highest SWE depth and yearly precipitation of any of the SNOTEL study locations.

Dominant vegetation was also assessed using the NLCD (Table 1; Homer et al., 2007). At Quemazon, the low elevation areas are dominated by grasslands, and the mid-to-high elevation areas are primarily shrub and evergreen forest. The majority of the forest was burned during the 2011 Las Conchas wildfire, thus grasses are now the dominant land cover. Truckee is located in the Sierra Nevada mountains, with predominantly evergreen forest. High elevation areas at Mt Ryan are primarily vegetated by evergreen forests, whereas the low elevation areas are primarily vegetated by shrubs. Similarly, Bettles is predominantly a mixture of evergreen forest and shrubs. Finally, the site on the Seward Peninsula is located on relatively low-relief hillslopes dominated by dwarf scrub (< 20 cm tall), tussock tundra, and a minor fraction of shrubs.

Table 1. The percentage vegetation cover in a 5 km^2 area surrounding each of the ASO and Landsat fSCA comparison sites according to the National Land Cover Dataset (Homer et al., 2007).

Location	**Evergreen Forest (%)**	**Deciduous Forest (%)**	**Mixed Forest (%)**	**Shrub (%)**	**Grassland (%)**	**Dwarf Scrub (%)**	**Tussock Tundra (%)**
Tuolumne Watershed, CA	38	n/a	n/a	55	7	n/a	n/a
Yuba River Watershed, CA	81	n/a	n/a	18	1	n/a	n/a
Blue River Watershed, CO	54	4	n/a	27	15	n/a	n/a
Conejos River Watershed, CO	43	14	n/a	31	12	n/a	n/a
Bettles Station SNOTEL	56	4	14	26	n/a	n/a	n/a
Mt. Ryan SNOTEL	58	2	2	39	n/a	n/a	n/a
Quemazon SNOTEL	15	n/a	n/a	18	68	n/a	n/a
Seward Site	n/a	n/a	n/a	4	n/a	88	8
Truckee SNOTEL	95	5	n/a	n/a	n/a	n/a	n/a

Table 2. The period of record averages for April 1st snow water equivalent (SWE), annual precipitation, and winter (DJF) temperatures at each SNOTEL station. The Seward site does not have an associated period of record at a nearby SNOTEL station, thus it is not included here.

Location	**Average April 1st SWE (cm)**	**Average Yearly Precipitation (cm)**	**Average Winter Temperature (C)**	**Period of Record**
Blue River watershed, Copper Mtn SNOTEL	37	73	-9	1986-present
Conejos River watershed, Lily Pond SNOTEL	33	77	-6	1981-present
Yuba River watershed, CSS Lab SNOTEL	85	173	-1	1988-present
Tuolumne River watershed, Dana Meadows snow course	75	n/a	n/a	1927-present
Bettles Station SNOTEL	17	42	-24	2001-present
Mt. Ryan SNOTEL	15	49	-15	1989-present
Quemazon SNOTEL	12	65	-4	1989-present
Truckee SNOTEL	40	89	0	1980-present

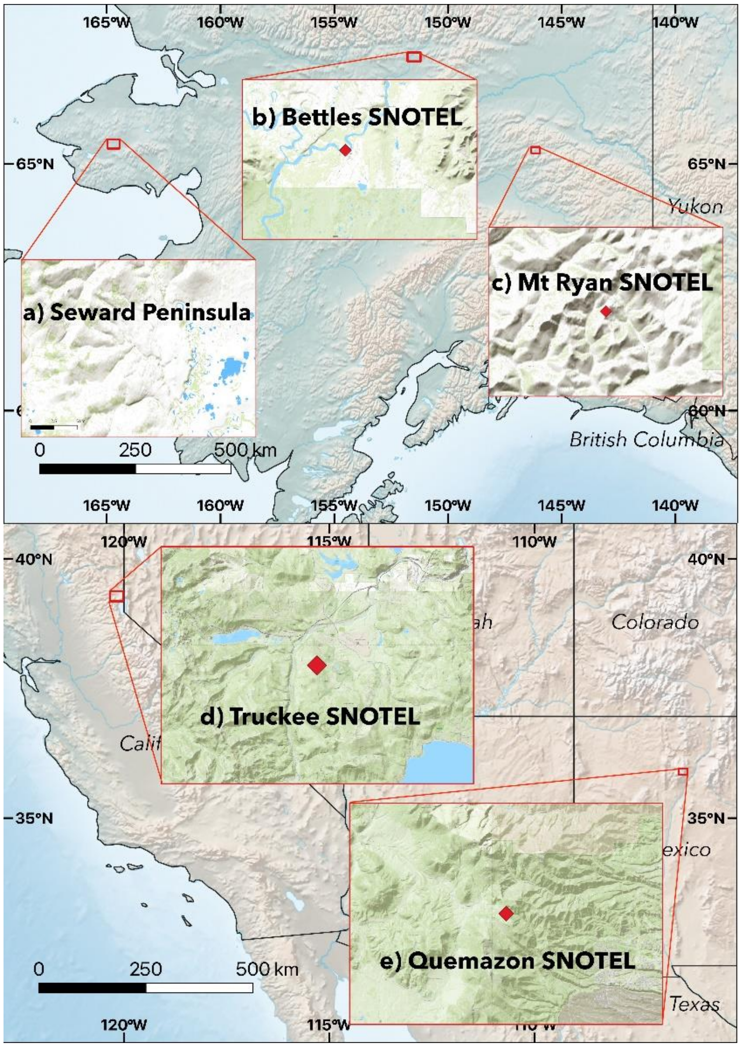

Figure 5. Study Area Map: **(a)** the Seward Peninsula region near Dahl, Alaska, **(b)** the Bettles region and SNOTEL station (Bettles Field #1182), **(c)** the Mt. Ryan region and SNOTEL station (Mt. Ryan #948), **(d)** the Truckee region and SNOTEL station (Truckee No.2 #834), and **(e)** the Quemazon region and SNOTEL station (Quemazon, #708).

We further validated BST-derived SCA by comparing end-of-season snow cover estimates to snow disappearance dates (SDD) from the SNOTEL stations. The SDDs at the SNOTEL stations were determined by choosing the first day the measured snow depth at the SNOTEL station record reaches 0 mm at the end of each snow season, with at least five subsequent days without the presence of snow (Crumley et al., 2020). The five-day threshold was chosen because there were multiple cases when late-season snowstorms added snow less than five days after the initial snow disappearance at the SNOTEL stations.

We generated a time series of SCA during the snowmelt season using the BST calculated from PlanetScope imagery for pixels within a 20 m radius of the SNOTEL station for the years 2017-2021. For each study location, except Mt Ryan, we generated the time series of SCAs for Spring 2021. At the Mt Ryan site, we generated the time series for Spring 2020 because the location was cloud-covered during most of the Spring 2021 snowmelt season. We then compared the BST-derived SCA to the in-situ snow depth measurements for several days leading up to the SDD determined for each SNOTEL station.

2.4 Comparison of the BST to Landsat fractional Snow-Covered Area

We compared BST-derived SCA from PlanetScope imagery to Landsat fSCA at each of the study locations in Figure 5 for paired images from 2017-2021. We use Landsat fSCA rather than SCA derived from Sentinel-2 NDSI because Landsat fSCA has been demonstrated to provide a modest accuracy increase compared to Sentinel-2 (Cannistra et al., 2021). The paired images were acquired within three days of each other, and for each image pair, we selected areas where the Landsat Revised Cloud Mask indicated the Landsat pixels were cloud-free. For each site, we chose images acquired during spring or late autumn to capture land areas with a mixture of SCA and non-SCA pixels.

At each study location, we calculated SCA within a 5 km^2 land area. We compared the areal extent of SCA predicted using BST to the total SCA predicted using Landsat fSCA. The total SCA predicted by BST was calculated by multiplying the number of pixels predicted to be snow-covered by the area of each pixel (9 m^2). To calculate the area of snow estimated by the Landsat fSCA product, we first used a threshold fSCA value of 0.15, such that only pixels with an fSCA > 0.15 were included in the calculation. We chose 0.15 as a threshold fSCA value because values < 0.15 can erroneously indicate snow, as the spectral signal of snow is dampened when mixed with non-snow pixels (Rittger et al., 2013). Then, we summed the product of each pixel value with a value > 0.15 and the area of each pixel (900 m^2), as shown by Equation 6,

$$\sum fSCA \cdot p_{area} \qquad (6)$$

where $fSCA$ is the dimensionless pixel value and p_{area} is the pixel area.

The dates of each BST-derived SCA and Landsat fSCA image pair can be found in Supplementary Material Table S1. At the Seward site, where high-resolution topographic data are available, we also examined the fine-scale differences in the SCA predictions within a topographic gully.

2.5 *Comparison of Planet and Landsat temporal availability*

To assess the differences in temporal availability of SCA estimates from the Landsat fSCA catalog and BST-derived SCA from Planet Labs imagery, we counted the number of cloud-free Landsat and Planet Labs images for each study site during the snow season of water year 2021. We determined the snow season using the SNOTEL snow depth record at each individual site. For the sites co-located with SNOTEL stations, the number of images was divided by the number of days that the station reported ≥ 254 mm of snow depth to calculate the percentage of snow-covered days with available imagery. At the Seward site, where there is no SNOTEL station, we considered the snow season to begin October 15 and end May 31, which is consistent with the snow season dates at Mt Ryan and Bettles, the two other high-latitude sites in Alaska. At the Alaska sites, image availability is limited between mid-October and mid-February, where sunlight is absent during image acquisition times. Therefore, we excluded these days from the percentage calculations for Mt Ryan, Bettles, and Seward. The number of snow season days with potential imagery ranges from 81 (Bettles) to 163 days (Truckee).

3. Results

3.1 Validation using airborne lidar surveys

The BST-derived SCA displays high accuracy when compared to the airborne lidar SCA maps in all four ALS sites (Figure 6). The maps in Figure 6 contain the lidar-derived SCA maps of snow cover extent at each of the ALS sites in California and Colorado overlain by the BST-derived SCA maps. Additionally, the scores from the prediction metrics as well as the true and false classification results are displayed in the corner of each map to clarify which pixels were classified correctly using the BST. The F-score for the BST-derived SCA prediction ranges from 0.81 to 0.94, with a mean value of 0.88 (Figure 6; Table 3). The balanced accuracies at the sites range from 0.79 to 0.86, with a mean of 0.81. There is broad agreement between the lidar-derived SCA maps and the BST-derived SCA maps across all sites even though they represent a range of climate regimes and land cover types (Tables 1 and 2).

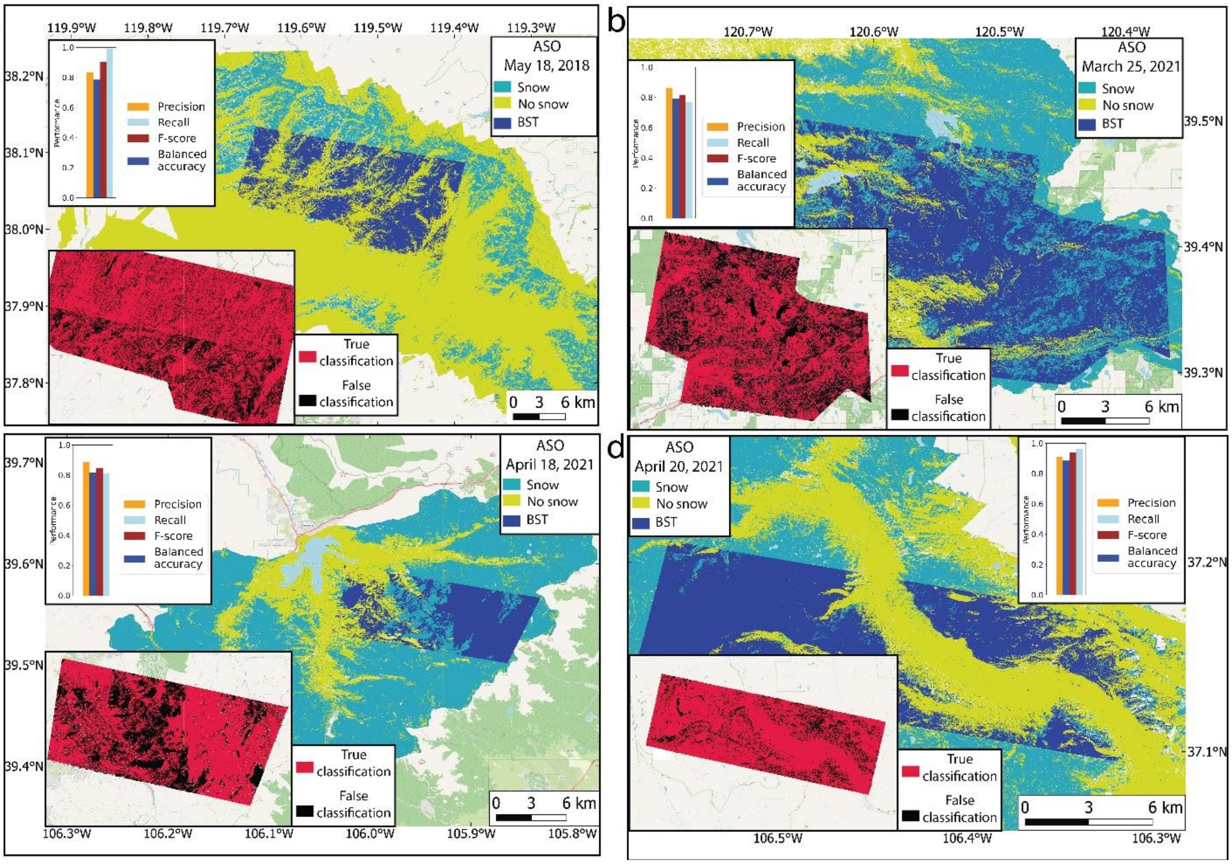

Figure 6. Snow-covered area (SCA) generated from the Blue Snow Threshold algorithm (BST) compared to lidar-derived SCA from the Airborne Snow Observatory (ASO) for **a)** Tuolumne River watershed, CA, **b)** Yuba River watershed, CA, **c)** Blue River watershed, CO, and **d)** Conejos River watershed, CO. In each panel the BST-derived SCA (dark blue polygons) is overlaid on the ASO snow mask, where light blue indicates snow and yellow indicates no snow. The map inset is zoomed in to the dark blue area and shows the true (red), or correctly classified pixels, and false (black) or incorrectly classified pixels. The bar chart inset shows the performance metrics, precision, recall, F-score, and balanced accuracy for each ASO site.

Table 3 Performance metrics of BST-derived SCA prediction compared to ASO-derived SCA "ground truth".

Location	**Precision**	**Recall**	**F-score**	**Balanced Accuracy**	**Analysis area (km^2)**	**ASO observation**	**Planet Scene ID**

Tuolumne River watershed CA	0.83	0.98	0.91	0.79	540	ASO_3M_SD_USCATE_20180528	20180528_181110_1025_3B 20180528_181111_1025_3B
Yuba River watershed CA	0.86	0.77	0.81	0.79	470	ASO_Yuba_Mosaic_2022Mar25	20220325_180813_96_2264_3B
Blue River watershed CO	0.89	0.81	0.85	0.81	205	ASO_BlueRiver_2021Apr18	20210419_171244_0e0f_3B
Conejos River watershed CO	0.91	0.96	0.94	0.86	363	ASO_Conejos_Mosaic_2021Apr20-21	20210420_173133_0f4e_3B

3.2 Validation using Landsat fSCA

Overall, the SCA estimated by Landsat fSCA are greater than the area predicted by the BST, with a mean difference over the five years of 18% to 66% at the study area sites (Figures 7,8; Table 4). However, within the topographic gully at the Seward site, the Landsat fSCA estimates a SCA of 0.061 km^2, while the BST predicts an area of 0.098 km^2 (Figure 9). Cloudless Planet images were significantly more numerous than Landsat fSCA images at each of the study sites. For example, during the 2021 water year, Planet images suitable for applying BST were available for 56% of the snow days during the snow season, on average (see Table 4 for individual study site calculations). By contrast, Landsat fSCA images were available for an average of 18% of the snow days during the snow season (Table 4). These results demonstrate that BST-derived SCA often calculates a different spatial extent than Landsat, and that BST-derived SCA images are available more frequently than Landsat-derived fSCA images.

Table 4. Comparison of Landsat fSCA and BST-derived SCA from PlanetScope satellite imagery. The percentage of cloud-free days of PlanetScope and Landsat imagery for water year 2021 are given for each site.

Location	**SCA difference between Landsat fSCA and BST (%)**	**Total number of days with potential for imagery**	**Percent of days of PlanetScope imagery**	**Percent of days with Landsat fSCA**
Quemazon SNOTEL	33	131	69	12
Truckee SNOTEL	66	163	51	11
Mt. Ryan SNOTEL	36	83	35	27
Bettles Station SNOTEL	30	81	60	26
Seward Site	18	95	67	13

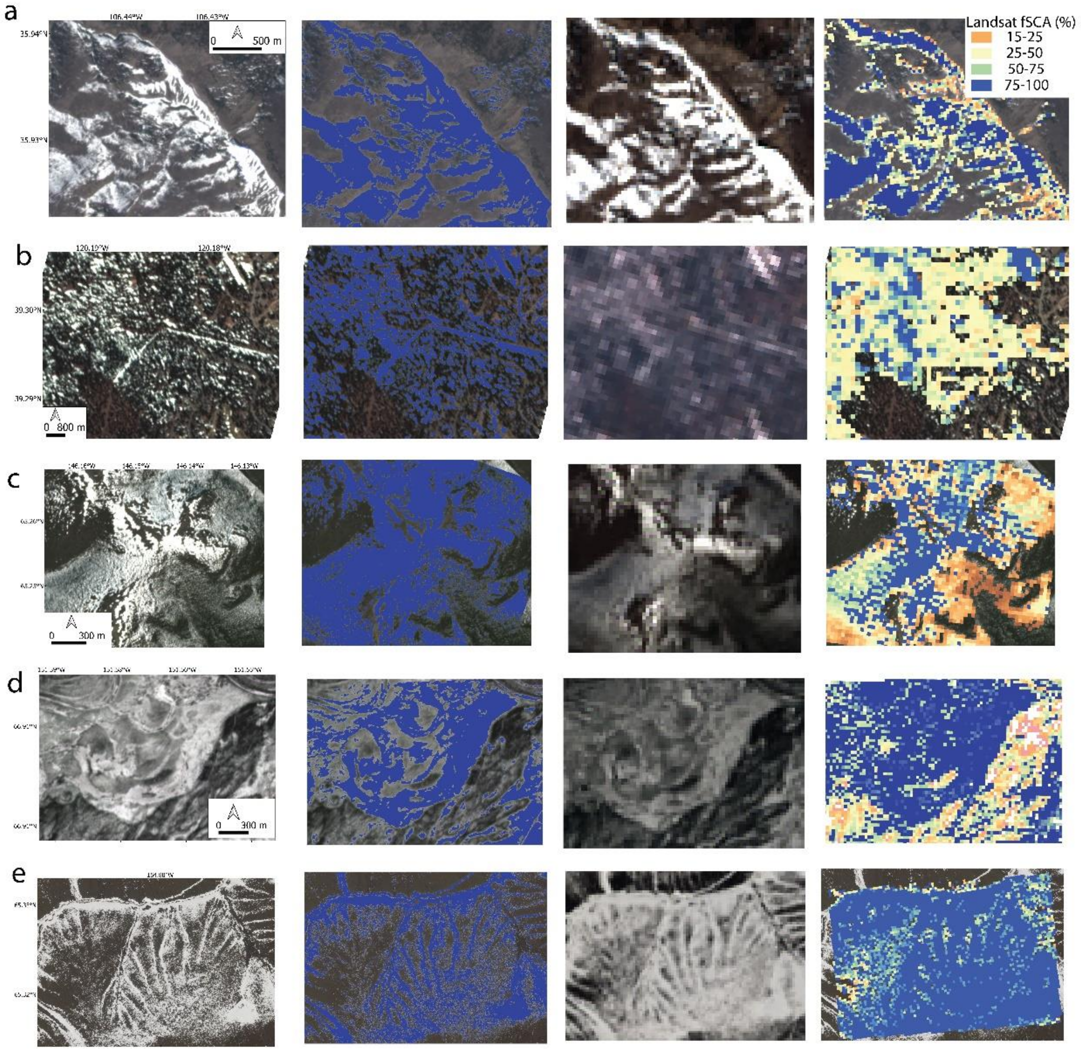

Figure 7. Example of high-resolution imagery, Landsat fractional snow-covered area (fSCA) and snow extent derived from the Blue Snow Threshold algorithm (BST) for a 5 km^2 from each of the five sites. The first column shows true color imagery, with snow indicated as the white pixels. The second column shows SCAs calculated using the BST, where blue pixels indicate snow and transparent pixels are areas lacking snow cover overlaid on the true color imagery. The third column shows the true color Landsat image. The fourth column shows estimates of snow area from the Landsat fSCA algorithm overlaid on the true color imagery. Transparent pixels indicate <15%, orange pixels represent 15-25%, yellow pixels indicate 25-50%, green pixels represent 50-75%, and blue pixels indicate 75-100% SCA. **(a)** Quemazon, NM **(b)** Truckee, CA **(c)** Mt Ryan, AK **(d)** Bettles, AK **(e)** Seward, AK.

3.3 Validation using snow telemetry stations

The comparison of BST-derived SDD and SDD at the SNOTEL sites displays broad agreement across all study sites. The SDD at the SNOTEL stations and BST-derived SDD from 2017 to 2021 are given in Table 5. For the time series analysis at the four stations, there is a consistent decrease in the timing of the SCA estimated from the BST and the measured snow depth at the SNOTEL station (Figure 10). The SNOTEL stations and the BST-derived SDD are in agreement at the Quemazon and Bettles sites. At the Truckee site, the BST indicates no SCA four days prior to the Snotel SDD, and one day prior to disappearance at the Mt Ryan site (Figure 10). The multi-year comparison of BST-derived SDD and SDD at the SNOTEL stations are consistent with the single year observations, where Quemazon is in agreement, the SDD is on average different by one day at Truckee, three days at Mt Ryan, and one day at Bettles. The Mt Ryan differences are partially due to the lack of cloud-free images available for the SDD estimated from the SNOTEL station.

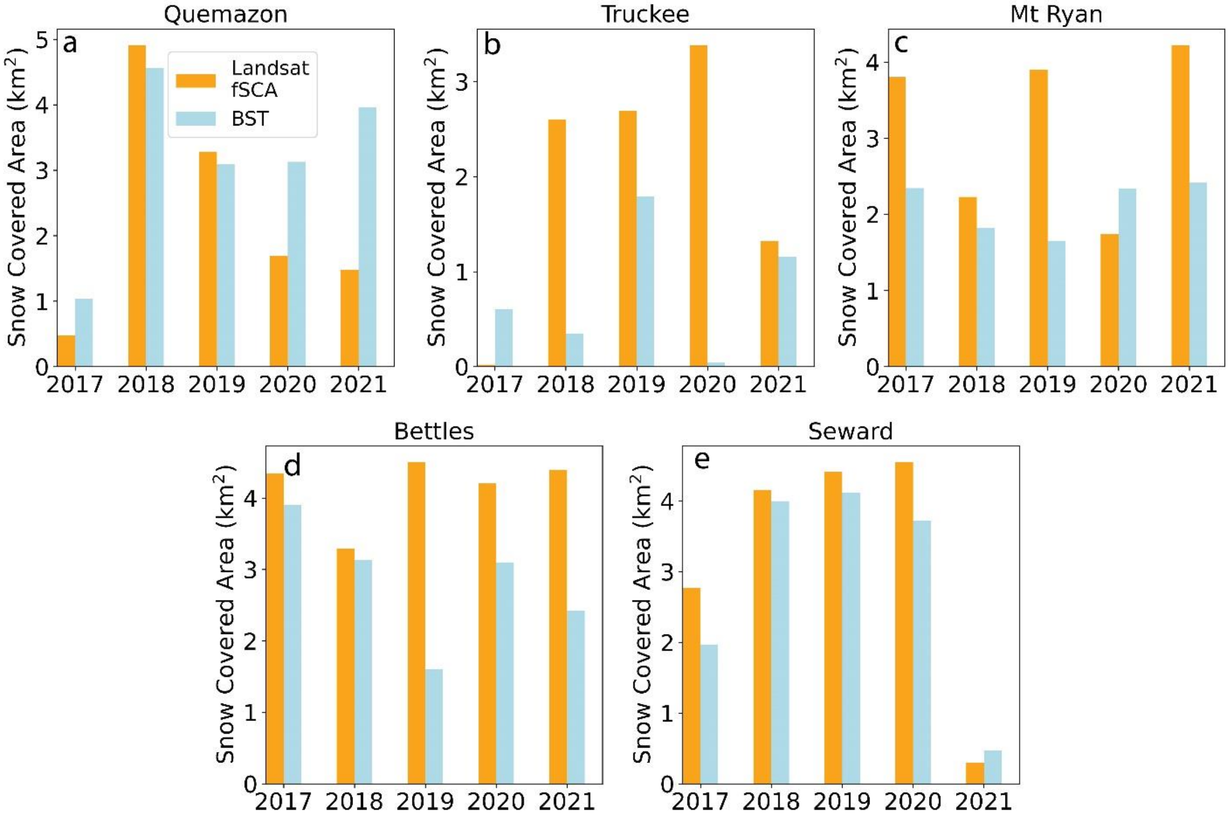

Figure 8. Comparison of snow-covered area predicted by the Blue Snow Threshold algorithm (BST, cyan bars) and the total snow-covered pixel area predicted by the Landsat Fractional Snow-Covered Area (fSCA, orange bars) for years 2017-2021. Only Landsat fSCA pixels with values >0.15 were included in the area calculation. Letters **(a-**

e) correspond to the letters in Figure 5. Each SCA extent was extracted from a 5 km^2 land area shown in Figure 7. The dates of the images from which SCA were derived are shown in Supplemental Table 1.

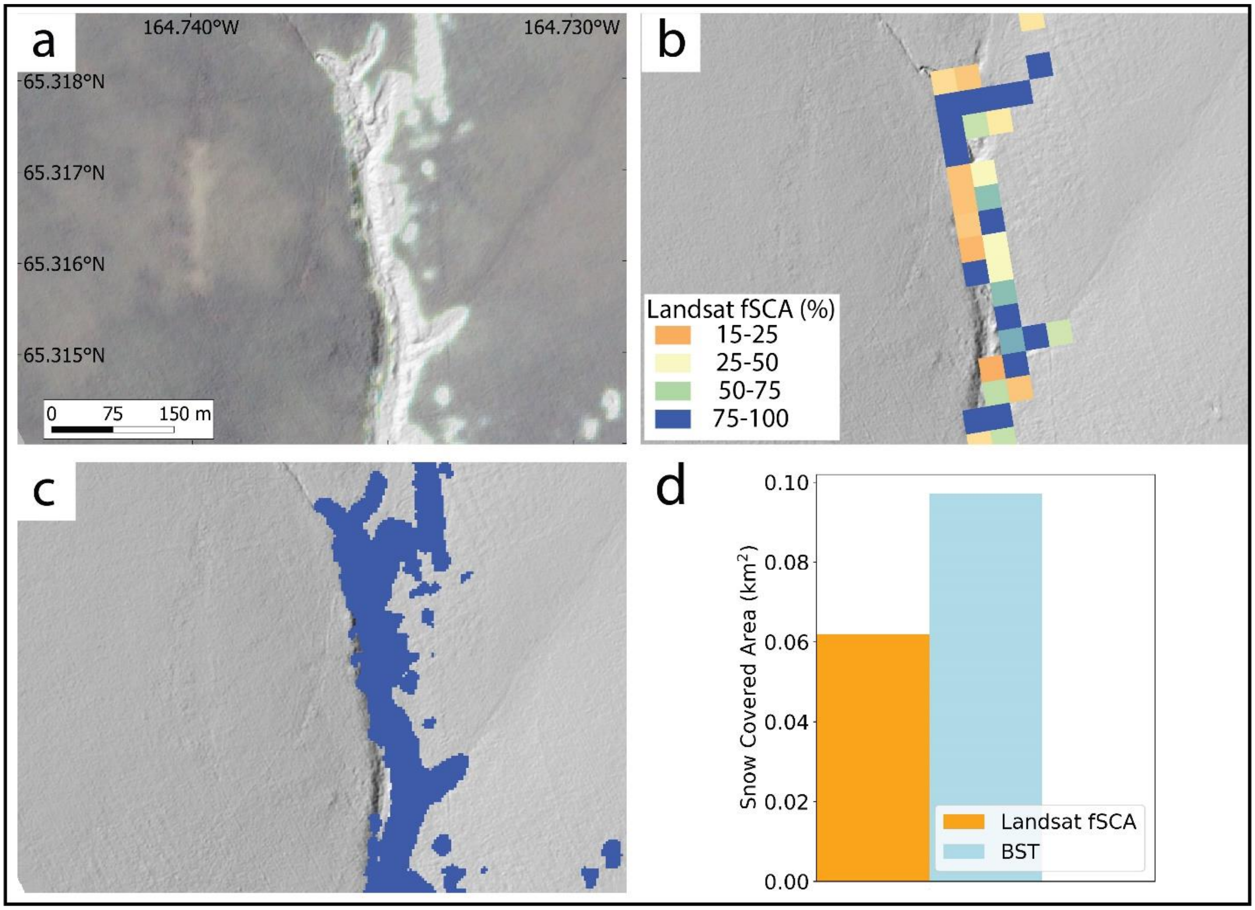

Figure 9. Example of the spatial resolution difference between snow-covered area (SCA) derived from the Landsat fractional snow-covered area (fSCA) algorithm and the Blue Snow Threshold algorithm (BST). **(a)** True color PlanetScope imagery overlaying lidar-derived hillshade raster of a topographic gully within the Seward, AK study site. **(b)** SCA estimated by the Landsat fSCA algorithm. **(c)** Snow-covered extent derived using the Blue Snow Threshold algorithm. (d) SCA predicted by Landsat fSCA (orange) and the BST (cyan). Landsat fSCA estimates a SCA of 0.061 km^2, while the BST predicts an area of 0.098 km^2.

Table 5. Dates of image acquisition for SNOTEL-derived snow disappearance date (SDD) the BST-derived SDD from 2017-2021. SNOTEL station numbers 708, 834, 948, 1182 correspond to Quemazon, Truckee, Mt Ryan, and Bettles Field, respectively.

Year	**SNOTEL SDD #708**	**BST SDD #708**	**SNOTEL SDD #834**	**BST SDD #834**	**SNOTEL SDD #948**	**BST SDD #948**	**SNOTEL SDD #1182**	**BST SDD #1182**
2017	4/6	4/6	5/22	5/24	5/10	5/10	5/13	5/11
2018	3/5	3/5	4/25	4/27	5/23	5/28 (Cloudy before)	5/21	5/21
2019	4/9	4/9	5/13	5/13	5/16	5/16	5/26	5/24
2020	4/1	4/2	4/30	4/30	5/18	5/17	5/21	5/20
2021	3/31	3/31	4/20	4/17	5/16	5/24 (cloudy before)	5/17	5/17

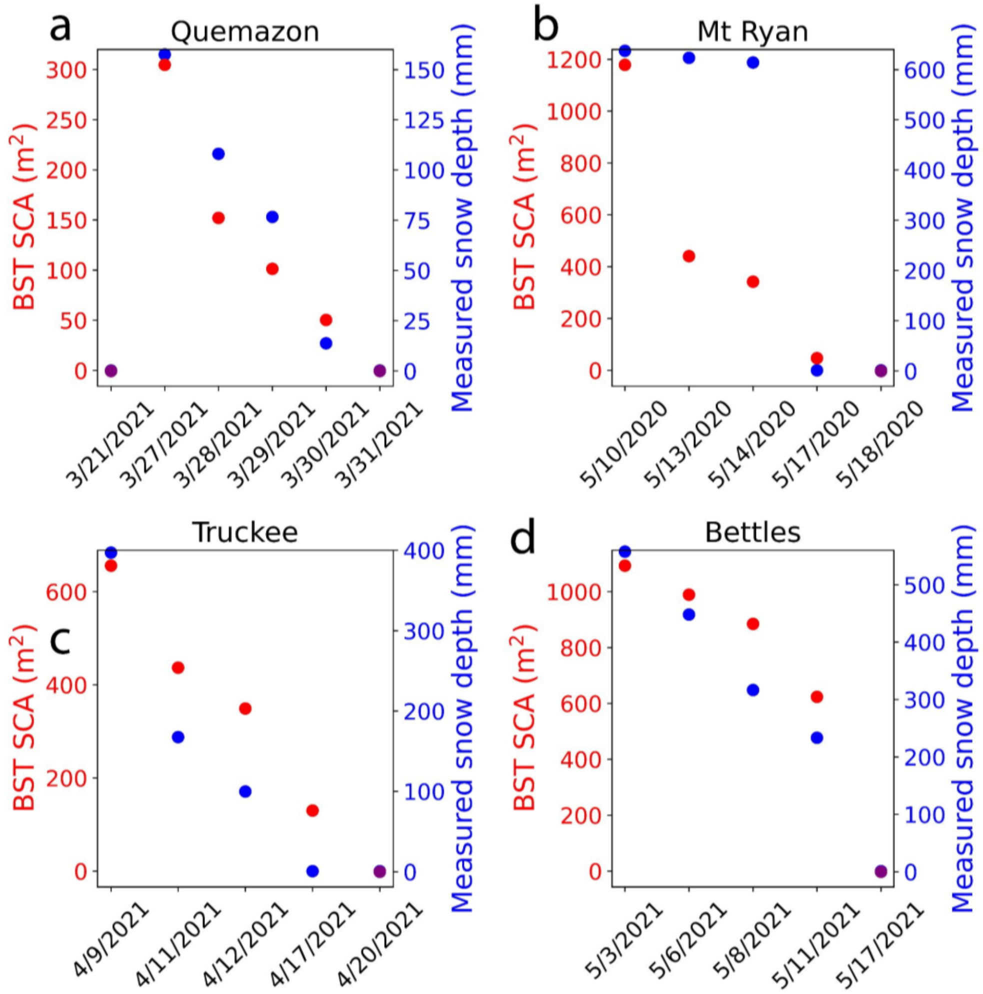

Figure 10. Estimation of snow extent (m^2, red points) using the Blue Snow Threshold algorithm (BST) and measured snow depth from the SNOTEL stations (mm, blue points). Purple points indicate measurements of zero for both parameters. **(a)** The Quemazon, NM Snotel station (708) near Valles Caldera, NM, **(b)** the Truckee #2 Snotel station (834) near Truckee, CA **(c)** the Mt Ryan Snotel station (948) near Fairbanks, AK, and **(d)** the Bettles Field Snotel station (1182) in the southern Brooks Range, AK. The areal snow extent estimates were calculated by summing the number of pixels classified as snow within a 20 m radius of the Snotel station.

4. Discussion

4.1 Advantages of the Blue Snow Threshold algorithm

The high F-scores for BST-derived SCA from high-resolution satellite imagery (Figure 6, Table 3) when compared to lidar-derived SCA suggests that BST is an effective method of generating SCA estimates solely using reflectance in the blue wavelengths. Further, the comparison of BST-derived SCA to Landsat fSCA and SDD derived from SNOTEL measurements indicates that BST can be used to estimate the precise timing and location of SCA, especially during the melt season when small scale variability of snow extent is high. The primary utility of the BST applied to high-resolution satellite imagery (3-5 m pixel resolution) is that it can effectively map SCA at spatial scales that are one to two orders of magnitude finer than other SCA products (i.e., MOD10A1=500 m, MODSCAG=500 m, Landsat fSCA=30 m) that require SWIR wavelengths, which are currently not measured by high-resolution sensors like those in the PlanetScope constellation.

We stress that BST performs well because it can be calculated from visible wavelengths measured by satellite sensors with very high spatial resolution, while the applicable resolution of NDSI is limited by the current spatial resolution of SWIR measurements. Further, we assert that if sufficient advances are made in the spatial resolution of SWIR measurements to match those in the visible spectrum, then NDSI would likely perform as well as the BST.

The advantages of mapping SCA at high-resolution can be demonstrated in locations like the Arctic, where complex topographic-driven patterns of end-of-season SCA are present (Callaghan et al., 2011; Parr et al., 2020; Sturm and Wagner, 2010). The BST method is particularly well-suited to Arctic and sub-Arctic landscapes dominated by relatively short tundra vegetation and in terrain where topographic shadows do not obscure the ground surface. The coarse resolution of SCA estimated by Landsat fSCA when compared to BST-derived SCA is demonstrated by the comparison of SCA for the two locations on the Seward Peninsula, which include the hillslope in Figure 7e and Figure 8e and the topographic gully shown in Figure 9. In the comparison site shown in Figure 7e, the coarse Landsat resolution results in many mixed snow and non-snow pixels, which are classified as snow by Landsat fSCA, but the higher resolution BST-derived SCA captures the subtle variability in snow cover, which is only clear at higher spatial resolutions. In the gully example (Figure 9), the Landsat fSCA resolution is too coarse to identify all of the snow-covered areas within the gully leading to an underprediction of SCA, whereas the BST calculated from the high-resolution satellite image identifies a greater SCA. The BST predicts a more nuanced distribution of snow at the hillslope scale when compared to Landsat fSCA, which indicates the suitability of the BST for assessing SCA at scales relevant to examining changing snow conditions on the snow-vegetation and snow-permafrost degradation feedbacks, which occur at the hillslope scale (Gisnås et al., 2014; Niittynen et al., 2020, 2018; Park et al., 2015).

Because BST-derived SCA can be generated at high resolutions (3m), it is less likely to contain mixed pixels than Landsat-derived fSCA (30m), particularly at the edge of forests or along the edges of other tall, dense vegetation or bare rock. Examining the performance of BST-derived SCA along the edge of forests is an important area of future research because the length of forest edges is an important control over preferential snow deposition in some climates (Dickerson-Lange et al., 2017; Dickerson-Lange et al., 2021). Unlike the Landsat fSCA product, a multiple endmember spectral unmixing algorithm is not used to produce BST-derived SCA. In locations where small-scale, mixed pixels may exist at the spatial resolution of BST-derived SCA, the BST is not likely to outperform the multiple endmember spectral unmixing method used in Landsat fSCA and can underpredict the SCA when compared to the fSCA algorithm, as demonstrated by the dramatic difference in SCA at the Truckee site (Figures 7b and 8b).

The BST is effective at the Quemazon site, which burned in 2011, where forest canopy cover has recently decreased and does not obscure satellite imagery from capturing the ground surface even though tree snags still exist. At this site, BST provides reasonable estimates of the SCA, which are comparable to the Landsat fSCA estimates (Figure 7a). Changes in forest structure in the Western U.S. have been affected by rapidly changing disturbance regimes, especially fires (McDowell et al., 2020). Forest cover alters snow accumulation mechanisms, as well as snowpack ablation rates, and affects the fine-scale variations in the distribution and duration of seasonal snow (Dickerson-Lange et al., 2017, 2021; Gleason et al., 2017; Lundquist et al., 2013). While we use imagery from Planet in this study, the BST can be applied to any true-color imagery like that available from other commercial satellites and aerial missions because it relies only on the blue wavelengths. A potential application of the BST is to apply the threshold to imagery captured by unpersonned aerial vehicles to estimate SCA in gaps in post-fire forested environments, locations that would not have been previously possible with low resolution SCA products. While the post-fire forested environment and forest gap analysis for BST-derived SCA was not within the scope of the present study, it is a promising area of future research.

Machine learning (ML) models recently developed from PlanetScope imagery have shown considerable promise in detecting and estimating SCA (Cannistra et al., 2021; John et al., 2022). While these recent advances in snow cover classification using ML models are important and useful, ML models perform best in the location where they are trained, and without site-specific training data their transferability may be limited. Generally, ML techniques work best when there is abundant data to train and validate the models, but snow science suffers from a general scarcity of high quality data related to snowpack in remote, expansive, and often inaccessible regions of the globe (Sturm, 2015). Because the BST is a simple, easy-to-apply algorithm that does not require a training dataset, it can be used in locations where training datasets are unavailable. However, an interesting avenue for future research is augmenting current ML models that use vegetation indices and elevation data with the BST to assess any potential accuracy improvement in the models.

Indexing based on spectral reflectance from optical remote sensing platforms (e.g., NDSI and fSCA from multiple endmember spectral unmixing) has, for decades, proven to be a simple and reliable tool for mapping SCA at coarse resolutions, in part because indexing does not require additional in-situ validation data (Dietz et al., 2012; Nolin, 2010; Sturm, 2015). Notably, at the Tuolumne ASO site, the prediction of SCA derived from the BST outperformed the ML method developed by Cannistra et al. (2021). The F-score of the BST prediction is 0.91, whereas the F-score of the ML prediction is 0.73. We note that we did not use the full set of Planet images in our analysis that were used to train and test the ML model by Cannistra et al. (2021); however, we still consider this comparison to be significant. Using BST to derive SCA adds another high-resolution effective method from optical remote sensing platforms that can be employed for expanding our understanding of the location, duration, and extent of SCA.

4.2 Limitations of the Blue Snow Threshold algorithm

The use of BST-derived SCA is limited by the same factors that limit other optical remote sensing techniques for snow cover classification. First, tall and dense vegetation, such as dense forest canopies, block optical remote sensing platforms from obtaining spectral reflectance information from below the forest canopy (Dietz et al., 2012; Nolin, 2010). For example, at the Truckee, Mt Ryan, and Bettles sites where vegetation is primarily tall coniferous tree species, the vegetation cover likely limits the visibility of the ground surface. In these areas, the BST likely underestimates the actual SCA, whereas fSCA algorithms can generate a canopy-adjustment by incorporating land use information (Figures 7 and 8). Hence fSCA algorithms may be better suited for SCA mapping in forested landscapes when using satellite-derived imagery (Barton et al., 2000; Raleigh et al., 2013), while the BST is well-suited for ecosystems like tundra, where vegetation height does not obscure the ground surface (Figure 9). Secondly, snowpacks are often located within high-relief, mountainous terrain where rugged topography can create shadowing effects due to slope, aspect, and winter sun angles, creating challenges for optical remote sensing platforms (Dozier, 1989, 1984). These shadows generated by the topography (e.g. Mt Ryan: Figure 7c) can cause the reflectance of snow in the blue wavelengths to be too low for BST to properly classify snow-covered pixels. Although there is potential to incorporate topographic data into the algorithm's workflow to improve SCA estimation in mountainous areas (e.g., John et al., 2022), we have not explored augmentation of the BST predictions using topographic data. Lastly, the optical remote sensing of snow, and therefore the BST, is hindered by the difficulty of discriminating between snow and clouds (Crane and Anderson, 1984.; Dietz et al., 2012; Dozier, 1989; Hall et al., 2002). In this work, we chose to only use cloud-free images in our analysis to avoid the complications of cloud and snow misclassification.

5. Conclusions

We generated estimates of snow-covered area (SCA) by calculating an existing binary index from cloud-free, high-resolution optical satellite imagery. While the most commonly used index for mapping snow cover, the normalized difference snow index (NDSI), relies on measurements in the short-wave infrared (SWIR) wavelengths, we present a binary SCA method, which we call the Blue Snow Threshold algorithm (BST), that relies only on spectral measurements in the blue wavelengths. SWIR wavelengths are typically only measured at coarse spatial resolution, so NDSI cannot be used to assess hillslope- or finer-scale distributions of snow, which are the scales relevant to examining important feedback processes, such as the snow-permafrost and snow-vegetation feedbacks. However, the BST-derived SCA from cloud-free, high-resolution satellite imagery, can be used to estimate snow extent at the hillslope scale or finer. When compared to airborne lidar surveys of SCA, the BST-derived SCA estimates had a range of F-scores between 0.81 and 0.94 in four study areas in California and Colorado. Furthermore, because of the temporal frequency of high-resolution image acquisition by commercial satellites, such as the Planet Labs constellation, the BST can be used to assess temporal trends in snow cover duration. The algorithm has the potential to be used to develop high spatiotemporal resolution maps of SCA which can be used to examine fine-scale changes in snow extent and duration related to changing climatic conditions.

Acknowledgements

We thank three anonymous reviewers and the editor, Menghua Wang, whose comments significantly improved the manuscript. Funding for this research was provided by the Department of Energy Office of Science, Office of Biological and Environmental Research through Next Generation Ecosystem Experiment (NGEE) Arctic project. The BST Python code is available upon request.

References

Aalstad, K., Westermann, S., Bertino, L., 2020. Evaluating satellite retrieved fractional snow-covered area at a high-Arctic site using terrestrial photography. Remote Sensing of Environment 239, 111618. https://doi.org/10.1016/j.rse.2019.111618

Adam, J.C., Hamlet, A.F., Lettenmaier, D.P., 2009. Implications of global climate change for snowmelt hydrology in the twenty-first century. Hydrological Processes 23, 962–972. https://doi.org/10.1002/hyp.7201

Barry, R.G., 1996. The parameterization of surface albedo for sea ice and its snow cover. Progress in Physical Geography 20, 63–79.

Barton, J.S., Hall, D.K., Riggs, G.A., 2000. Remote sensing of fractional snow cover using Moderate Resolution Imaging Spectroradiometer (MODIS) data, in: Proceedings of the 57th Eastern Snow Conference. pp. 171–183.

Bennett, K.E., Cherry, J.E., Balk, B., Lindsey, S., 2019. Using MODIS estimates of fractional snow cover area to improve streamflow forecasts in interior Alaska. Hydrology and Earth System Sciences 23, 2439–2459. https://doi.org/10.5194/hess-23-2439-2019

Bennett, K.E., Miller, G., Busey, R., Chen, M., Lathrop, E.R., Dann, J.B., Nutt, M., Crumley, R., Dafflon, B., Kumar, J. and Bolton, W.R., 2021. Spatial Patterns of Snow Distribution for Improved Earth System Modelling in the Arctic. *The Cryosphere Discussions*, pp.1-44. https://doi.org/10.5194/tc-2021-341

Biskaborn, B.K., Smith, S.L., Noetzli, J., Matthes, H., Vieira, G., Streletskiy, D.A., Schoeneich, P., Romanovsky, V.E., Lewkowicz, A.G., Abramov, A., Allard, M., Boike, J., Cable, W.L., Christiansen, H.H., Delaloye, R., Diekmann, B., Drozdov, D., Etzelmüller, B., Grosse, G., Guglielmin, M., Ingeman-Nielsen, T., Isaksen, K., Ishikawa, M., Johansson, M., Johannsson, H., Joo, A., Kaverin, D., Kholodov, A., Konstantinov, P., Kröger, T., Lambiel, C., Lanckman, J.-P., Luo, D., Malkova, G., Meiklejohn, I., Moskalenko, N., Oliva, M., Phillips, M., Ramos, M., Sannel, A.B.K., Sergeev, D., Seybold, C., Skryabin, P., Vasiliev, A., Wu, Q., Yoshikawa, K., Zheleznyak, M., Lantuit, H., 2019. Permafrost is warming at a global scale. Nat Comm. 10, 264. https://doi.org/10.1038/s41467-018-08240-4

Budyko, M.I., 1969. The effect of solar radiation variations on the climate of the Earth. Tellus 21, 611–619. https://doi.org/10.1111/j.2153-3490.1969.tb00466.x

Callaghan, T.V., Johansson, M., Brown, R.D., Groisman, P.Y., Labba, N., Radionov, V., Bradley, R.S., Blangy, S., Bulygina, O.N., Christensen, T.R., 2011. Multiple effects of changes in Arctic snow cover. Ambio 40, 32–45.

Cannistra, A.F., Shean, D.E., Cristea, N.C., 2021. High-resolution CubeSat imagery and machine learning for detailed snow-covered area. Remote Sensing of Environment 258, 112399. https://doi.org/10.1016/j.rse.2021.112399

Crane, R.G. and Anderson, M.R., 1984. Satellite discrimination of snow/cloud surfaces. *International Journal of Remote Sensing*, *5*, 213-223

Crumley, R.L., Palomaki, R.T., Nolin, A.W., Sproles, E.A., Mar, E.J., 2020. SnowCloudMetrics: Snow Information for Everyone. Remote Sensing 12, 3341. https://doi.org/10.3390/rs12203341

Déry, S.J., Brown, R.D., 2007. Recent Northern Hemisphere snow cover extent trends and implications for the snow-albedo feedback. Geophys. Res. Lett. 34, L22504. https://doi.org/10.1029/2007GL031474

Dickerson-Lange, S.E., Gersonde, R.F., Hubbart, J.A., Link, T.E., Nolin, A.W., Perry, G.H., Roth, T.R., Wayand, N.E. and Lundquist, J.D., 2017. Snow disappearance timing is dominated by forest effects on snow accumulation in warm winter climates of the Pacific Northwest, United States. *Hydrological Processes*, *31*, 1846-1862

Dickerson-Lange, S.E., Vano, J.A., Gersonde, R., Lundquist, J.D., 2021. Ranking Forest Effects on Snow Storage: A Decision Tool for Forest Management. Water Resources Research 57, e2020WR027926. https://doi.org/10.1029/2020WR027926

Dietz, A.J., Kuenzer, C., Gessner, U., Dech, S., 2012. Remote sensing of snow – a review of available methods. International Journal of Remote Sensing 33, 4094–4134. https://doi.org/10.1080/01431161.2011.640964

Dong, C., 2018. Remote sensing, hydrological modeling and in situ observations in snow cover research: A review. Journal of Hydrology 561, 573–583. https://doi.org/10.1016/j.jhydrol.2018.04.027

Dozier, J., 1989. Spectral signature of alpine snow cover from the landsat thematic mapper. Remote Sensing of Environment 28, 9–22. https://doi.org/10.1016/0034-4257(89)90101-6

Dozier, J., 1984. Snow Reflectance from LANDSAT-4 Thematic Mapper. IEEE Transactions on Geoscience and Remote Sensing GE-22, 323–328. https://doi.org/10.1109/TGRS.1984.350628

Fedorov, R., Camerada, A., Fraternali, P., Tagliasacchi, M., 2016. Estimating snow cover from publicly available images. IEEE Trans. Multimedia 18, 1187–1200. https://doi.org/10.1109/TMM.2016.2535356

Frazier, A.E., Hemingway, B.L., 2021. A technical review of planet smallsat data: Practical considerations for processing and using planetscope imagery. Remote Sensing 13, 3930.

Gascoin, S., Barrou Dumont, Z., Deschamps-Berger, C., Marti, F., Salgues, G., López-Moreno, J.I., Revuelto, J., Michon, T., Schattan, P., Hagolle, O., 2020. Estimating fractional snow cover in open terrain from sentinel-2 using the normalized difference snow index. Remote Sensing 12, 2904.

Gisnås, K., Westermann, S., Schuler, T.V., Litherland, T., Isaksen, K., Boike, J., Etzelmüller, B., 2014. A statistical approach to represent small-scale variability of permafrost temperatures due to snow cover. The Cryosphere 8, 2063–2074. https://doi.org/10.5194/tc-8-2063-2014

Gleason, K.E., Nolin, A.W., Roth, T.R., 2017. Developing a representative snow-monitoring network in a forested mountain watershed. Hydrology and Earth System Sciences 21, 1137–1147. https://doi.org/10.5194/hess-21-1137-2017

Groisman, P.Y., Karl, T.R., Knight, R.W., Stenchikov, G.L., 1994. Changes of Snow Cover, Temperature, and Radiative Heat Balance over the Northern Hemisphere. Journal of Climate 7, 1633–1656. https://doi.org/10.1175/1520-0442(1994)007<1633:COSCTA>2.0.CO;2

Hall, D., Riggs, G., 2021. MODIS/Terra Snow Cover 5-Min L2 Swath 500m, Version 61 [on-line]. Bm: NASA National Snow and Ice Data Center DAAC.

Hall, D.K., Riggs, G.A., Salomonson, V.V., DiGirolamo, N.E., Bayr, K.J., 2002. MODIS snow-cover products. Remote Sensing of Environment, The Moderate Resolution Imaging Spectroradiometer (MODIS): a new generation of Land Surface Monitoring 83, 181–194. https://doi.org/10.1016/S0034-4257(02)00095-0

Hartigan, P. M. (1985). Computation of the Dip Statistic to Test for Unimodality. Journal of the Royal Statistical Society. Series C (Applied Statistics), 34(3), 320-325.

Homer, C., Dewitz, J., Fry, J., Coan, M., Hossain, N., Larson, C., Herold, N., McKerrow, A., VanDriel, J.N., Wickham, J., others, 2007. Completion of the 2001 national land cover database for the conterminous United States. Photogrammetric engineering and remote sensing 73, 337.

Hu, J.M. and Shean, D., 2022. Improving Mountain Snow and Land Cover Mapping Using Very-High-Resolution (VHR) Optical Satellite Images and Random Forest Machine Learning Models. *Remote Sensing*, *14*(17), p.4227.

John, A., Cannistra, A.F., Yang, K., Tan, A., Shean, D., Hille Ris Lambers, J., Cristea, N., 2022. High-Resolution Snow-Covered Area Mapping in Forested Mountain Ecosystems Using PlanetScope Imagery. Remote Sensing 14, 3409.

Kelsey, K.C., Pedersen, S.H., Leffler, A.J., Sexton, J.O., Feng, M., Welker, J.M., 2021. Winter snow and spring temperature have differential effects on vegetation phenology and productivity across Arctic plant communities. Glob. Change Biol. 27, 1572–1586. https://doi.org/10.1111/gcb.15505

Kostadinov, T.S., Schumer, R., Hausner, M., Bormann, K.J., Gaffney, R., McGwire, K., Painter, T.H., Tyler, S., Harpold, A.A., 2019. Watershed-scale mapping of fractional snow cover under conifer forest canopy using lidar. Remote Sensing of Environment 222, 34–49.

Lillesand, T., Kiefer, R.W., Chipman, J., 2015. Remote sensing and image interpretation. John Wiley & Sons.

Liston, G.E., Hiemstra, C.A., 2011. The Changing Cryosphere: Pan-Arctic Snow Trends (1979–2009). Journal of Climate 24, 5691–5712. https://doi.org/10.1175/JCLI-D-11-00081.1

Lundquist, J.D., Dickerson-Lange, S.E., Lutz, J.A., Cristea, N.C., 2013. Lower forest density enhances snow retention in regions with warmer winters: A global framework developed from plot-scale observations and modeling. Water Resources Research 49, 6356–6370. https://doi.org/10.1002/wrcr.20504

Marta, S., 2018. Planet imagery product specifications. Planet Labs: San Francisco, CA, USA 91.

Matson, M., Wiesnet, D.R., 1981. New data base for climate studies. Nature, 451–456. https://doi.org/10.1038/289451a0

McDowell, N.G., Allen, C.D., Anderson-Teixeira, K., Aukema, B.H., Bond-Lamberty, B., Chini, L., Clark, J.S., Dietze, M., Grossiord, C., Hanbury-Brown, A., Hurtt, G.C., Jackson, R.B., Johnson, D.J., Kueppers, L., Lichstein, J.W., Ogle, K., Poulter, B., Pugh, T.A.M., Seidl, R., Turner, M.G., Uriarte, M., Walker, A.P., Xu, C., 2020. Pervasive shifts in forest dynamics in a changing world. Science 368. https://doi.org/10.1126/science.aaz9463

Meerdink, S.K., Hook, S.J., Roberts, D.A., Abbott, E.A., 2019. The ECOSTRESS spectral library version 1.0. Remote Sensing of Environment 230, 111196.

Mekonnen, Z.A., Riley, W.J., Berner, L.T., Bouskill, N.J., Torn, M.S., Iwahana, G., Breen, A.L., Myers-Smith, I.H., Criado, M.G., Liu, Y., Euskirchen, E.S., Goetz, S.J., Mack, M.C., Grant, R.F., 2021. Arctic tundra shrubification: a review of mechanisms and impacts on ecosystem carbon balance. Environ. Res. Lett. 16, 053001. https://doi.org/10.1088/1748-9326/abf28b

Mote, P.W., Hamlet, A.F., Clark, M.P., Lettenmaier, D.P., 2005. Declining mountain snowpack in Western North America. Bull. Amer. Meteor. Soc. 86, 39–50. https://doi.org/10.1175/BAMS-86-1-39

Muhuri, A., Gascoin, S., Menzel, L., Kostadinov, T.S., Harpold, A.A., Sanmiguel-Vallelado, A., López-Moreno, J.I., 2021. Performance Assessment of Optical Satellite-Based Operational Snow Cover Monitoring Algorithms in Forested Landscapes. IEEE Journal of Selected Topics in Applied Earth Observations and Remote Sensing 14, 7159–7178.

Nagler, T., Rott, H., Ripper, E., Bippus, G., Hetzenecker, M., 2016. Advancements for snowmelt monitoring by means of Sentinel-1 SAR. Remote Sensing 8, 348.

Neigh, C.S.R., Masek, J.G., Nickeson, J.E., 2013. High-Resolution Satellite Data Open for Government Research. Eos Trans. AGU 94, 121–123. https://doi.org/10.1002/2013EO130002

Niittynen, P., Heikkinen, R.K., Luoto, M., 2020. Decreasing snow cover alters functional composition and diversity of Arctic tundra. Proc Natl Acad Sci USA 117, 21480–21487. https://doi.org/10.1073/pnas.2001254117

Niittynen, P., Heikkinen, R.K., Luoto, M., 2018. Snow cover is a neglected driver of Arctic biodiversity loss. Nature Clim Change 8, 997–1001. https://doi.org/10.1038/s41558-018-0311-x

Nolin, A.W., 2010. Recent advances in remote sensing of seasonal snow. J. Glaciol. 56, 1141–1150. https://doi.org/10.3189/002214311796406077

Nolin, A.W., Dozier, J., Mertes, L.A., 1993. Mapping alpine snow using a spectral mixture modeling technique. Annals of Glaciology 17, 121–124.

Painter, T.H., Berisford, D.F., Boardman, J.W., Bormann, K.J., Deems, J.S., Gehrke, F., Hedrick, A., Joyce, M., Laidlaw, R., Marks, D., Mattmann, C., McGurk, B., Ramirez, P., Richardson, M., Skiles, S.M., Seidel, F.C., Winstral, A., 2016. The Airborne Snow Observatory: Fusion of scanning lidar, imaging spectrometer, and physically-based modeling for mapping snow water equivalent and snow albedo. Remote Sensing of Environment 184, 139–152. https://doi.org/10.1016/j.rse.2016.06.018

Painter, T.H., Rittger, K., McKenzie, C., Slaughter, P., Davis, R.E., Dozier, J., 2009. Retrieval of subpixel snow covered area, grain size, and albedo from MODIS. Remote Sensing of Environment 113, 868–879. https://doi.org/10.1016/j.rse.2009.01.001

Park, H., Fedorov, A.N., Zheleznyak, M.N., Konstantinov, P.Y., Walsh, J.E., 2015. Effect of snow cover on pan-Arctic permafrost thermal regimes. Clim Dyn 44, 2873–2895. https://doi.org/10.1007/s00382-014-2356-5

Parr, C., Sturm, M., Larsen, C., 2020. Snowdrift landscape patterns: An Arctic investigation. Water Resources Research 56, e2020WR027823.

Raleigh, M.S., Rittger, K., Moore, C.E., Henn, B., Lutz, J.A., Lundquist, J.D., 2013. Ground-based testing of MODIS fractional snow cover in subalpine meadows and forests of the Sierra Nevada. Remote Sensing of Environment 128, 44–57.

Rango, A., Itten, K., 1976. Satellite potentials in snowcover monitoring and runoff prediction. Hydrology Research 7, 209–230.

Rittger, K., Painter, T.H., Dozier, J., 2013. Assessment of methods for mapping snow cover from MODIS. Advances in Water Resources 51, 367–380. https://doi.org/10.1016/j.advwatres.2012.03.002

Robinson, D.A., Dewey, K.F., Heim, R.R., 1993. Global Snow Cover Monitoring: An Update. Bulletin of the American Meteorological Society 74, 1689–1696.

Salomonson, V.V., Appel, I., 2004. Estimating fractional snow cover from MODIS using the normalized difference snow index. Remote Sensing of Environment 89, 351–360. https://doi.org/10.1016/j.rse.2003.10.016

Salvatori, R., Plini, P., Giusto, M., Valt, M., Salzano, R., Montagnoli, M., Cagnati, A., Crepaz, G., Sigismondi, D., 2011. Snow cover monitoring with images from digital camera systems. ItJRS 137–145. https://doi.org/10.5721/ItJRS201143211

Salzano, R., Salvatori, R., Valt, M., Giuliani, G., Chatenoux, B., Ioppi, L., 2019. Automated classification of terrestrial images: The contribution to the remote sensing of snow cover. Geosciences 9, 97.

Schmidt, N.M., Reneerkens, J., Christensen, J.H., Olesen, M., Roslin, T., 2019. An ecosystem-wide reproductive failure with more snow in the Arctic. PLOS Biology 17, e3000392. https://doi.org/10.1371/journal.pbio.3000392

Selkowitz, D.J., Forster, R.R., 2016. Automated mapping of persistent ice and snow cover across the western U.S. with Landsat. ISPRS Journal of Photogrammetry and Remote Sensing 117, 126–140. https://doi.org/10.1016/j.isprsjprs.2016.04.001

Selkowitz, D.J., Painter, T.H., Rittger, K.E., Schmidt, G. and Forster, R., 2017. The USGS Landsat Snow Covered Area Products: Methods and Preliminary Validation. *Automated Approaches for Snow and Ice Cover Monitoring Using Optical Remote Sensing; University of Utah: Salt Lake City, UT, USA*, pp.76-119.

Sellers, W.D., 1969. A Global Climatic Model Based on the Energy Balance of the Earth-Atmosphere System. Journal of Applied Meteorology and Climatology 8, 392–400.

Smith, S.L., O’Neill, H.B., Isaksen, K., Noetzli, J., Romanovsky, V.E., 2022. The changing thermal state of permafrost. Nat Rev Earth Environ 3, 10–23. https://doi.org/10.1038/s43017-021-00240-1

Stewart, I.T., Cayan, D.R., Dettinger, M.D., 2005. Changes toward Earlier Streamflow

Timing across Western North America. Journal of Climate 18, 1136–1155. https://doi.org/10.1175/JCLI3321.1

Sturm, M., 2015. White water: Fifty years of snow research in WRR and the outlook for the future. Water Resources Research 51, 4948–4965. https://doi.org/10.1002/2015WR017242

Sturm, M., Wagner, A.M., 2010. Using repeated patterns in snow distribution modeling: An Arctic example. Water Resour. Res. 46. https://doi.org/10.1029/2010WR009434

Thackeray, C.W., Fletcher, C.G., 2016. Snow albedo feedback: Current knowledge, importance, outstanding issues and future directions. Progress in Physical Geography: Earth and Environment 40, 392–408. https://doi.org/10.1177/0309133315620999

Tsai, Y.-L.S., Dietz, A., Oppelt, N., Kuenzer, C., 2019. Remote sensing of snow cover using spaceborne SAR: A review. Remote Sensing 11, 1456.

Uhlemann, S., Dafflon, B., Peterson, J., Ulrich, C., Shirley, I., Michail, S., Hubbard, S.S., 2021. Geophysical monitoring shows that spatial heterogeneity in thermohydrological dynamics reshapes a transitional permafrost system. Geophysical Research Letters 48, e2020GL091149.

Wiesnet, D.R., Ropelewski, C.F., Kukla, G.J. and Robinson, D.A., 1987. A discussion of the accuracy of NOAA satellite-derived global seasonal snow cover measurements. *Large Scale Effects of Seasonal Snow Cover*, *166*, pp.291-304.

Wilcox, E.J., Keim, D., de Jong, T., Walker, B., Sonnentag, O., Sniderhan, A.E., Mann, P., Marsh, P., 2019. Tundra shrub expansion may amplify permafrost thaw by advancing snowmelt timing. Arctic Science 5, 202–217. https://doi.org/10.1139/as-2018-0028

Zhang, T., 2005. Influence of the seasonal snow cover on the ground thermal regime: An overview. Reviews of Geophysics 43. https://doi.org/10.1029/2004RG000157

Zhang, T., Osterkamp, T.E., Stamnes, K., 1997. Effects of Climate on the Active Layer and Permafrost on the North Slope of Alaska, U.S.A. Permafrost and Periglacial Processes 8, 45–67.

List of Figure Captions

Figure 1. Examples of spectral curves for common natural materials. The blue, green, and gray shaded area indicate the blue, green, and shortwave infrared wavelengths, respectively. Within the blue wavelengths, coarse granular snow has a nearly 80% greater reflectance than the other natural objects. Spectral data are from the Ecostress Spectral Library (Meerdink et al., 2019).

Figure 2. Flow chart demonstrating the automated threshold (*t*) calculation procedure of the Blue Snow Threshold algorithm. Images with a high percentage of snow cover

follow the left side of the chart, and images with mixed snow and non-snow pixels follow the right side of the chart.

Figure 3. Example of the threshold selection for binary classification of pixels using the Blue Snow Threshold algorithm (BST). The image is a 16-bit surface reflectance product, which is scaled by a factor of 10,000. a) Example of threshold selection for an image primarily composed of snow-covered pixels. PlanetScope true-color satellite image of a location on the Seward Peninsula (see Figure 5a) acquired on March 04, 2020. b) Distribution of ρ_{blue} values from the snow-covered image. In this image $\overline{\rho_{blue}}$ is 0.86 (8,600), which is > $\overline{\rho_{blue}}$ defined by the algorithm for mixed snow non-snow images (0.70); therefore, *t* is set to the fixed value of 0.70 (7,000) c) Snow mask generated from the BST. Blue pixels indicate those classified as snow. d) PlanetScope true-color satellite image of a location on the Seward Peninsula (see Figure 5a) acquired on May 05, 2020. e) Smoothed distribution of ρ_{blue} values from the image with the threshold shown as the blue dashed line. The threshold (*t*) in this example is 0.37 (3,700). Values greater than the threshold are considered snow, whereas values less than the threshold are non-snow pixels. f) Snow mask generated from the BST. Blue areas indicate pixels classified as snow.

Figure 4. Airborne lidar surveys map: **(a)** the Yuba River and Tuolumne River watersheds in California, and **(b)** the Blue River and Conejos River watersheds in Colorado where the Airborne Snow Observatory acquired lidar datasets of snow depth for multiple years.

Figure 5. Study Area Map: **(a)** the Seward Peninsula region near Dahl, Alaska, **(b)** the Bettles region and SNOTEL station (Bettles Field #1182), **(c)** the Mt. Ryan region and SNOTEL station (Mt. Ryan #948), **(d)** the Truckee region and SNOTEL station (Truckee No.2 #834), and **(e)** the Quemazon region and SNOTEL station (Quemazon, #708).

Figure 6. Snow-covered area (SCA) generated from the Blue Snow Threshold algorithm (BST) compared to lidar-derived SCA from the Airborne Snow Observatory (ASO) for **a)** Tuolumne River watershed, CA, **b)** Yuba River watershed, CA, **c)** Blue River watershed, CO, and **d)** Conejos River watershed, CO. In each panel the BST-derived SCA (dark blue polygons) is overlaid on the ASO snow mask, where light blue indicates snow and yellow indicates no snow. The map inset is zoomed in to the dark blue area and shows the true (red), or correctly classified pixels, and false (black) or incorrectly classified pixels. The bar chart inset shows the performance metrics, precision, recall, F-score, and balanced accuracy for each ASO site.

Figure 7. Example of high-resolution imagery, Landsat fractional snow-covered area (fSCA) and snow extent derived from the Blue Snow Threshold algorithm (BST) for a 5 km^2 from each of the five sites. The first column shows true color imagery, with snow indicated as the white pixels. The second column shows SCAs calculated using the BST, where blue pixels indicate snow and transparent pixels are areas lacking snow cover overlaid on the true color imagery. The third column shows the true color Landsat image. The fourth column shows estimates of snow area from the Landsat fSCA algorithm overlaid on the true color imagery. Transparent pixels indicate <15%, orange pixels represent 15-25%, yellow pixels indicate 25-50%, green pixels represent 50-75%, and blue pixels indicate 75-100% SCA. **(a)** Quemazon, NM **(b)** Truckee, CA **(c)** Mt Ryan, AK **(d)** Bettles, AK **(e)** Seward, AK.

Figure 8. Comparison of snow-covered area predicted by the Blue Snow Threshold algorithm (BST, cyan bars) and the total snow-covered pixel area predicted by the Landsat Fractional Snow-Covered Area (fSCA, orange bars) for years 2017-2021. Only Landsat fSCA pixels with values >0.15 were included in the area calculation. Letters **(a-e)** correspond to the letters in Figure 5. Each SCA extent was extracted from a 5 km^2 land area shown in Figure 7. The dates of the images from which SCA were derived are shown in Supplemental Table 1.

Figure 9. Example of the spatial resolution difference between snow-covered area (SCA) derived from the Landsat fractional snow-covered area (fSCA) algorithm and the Blue Snow Threshold algorithm (BST). **(a)** True color PlanetScope imagery overlaying lidar-derived hillshade raster of a topographic gully within the Seward, AK study site. **(b)** SCA estimated by the Landsat fSCA algorithm. **(c)** Snow-covered extent derived using the Blue Snow Threshold algorithm. (d) SCA predicted by Landsat fSCA (orange) and the BST (cyan). Landsat fSCA estimates a SCA of 0.061 km^2, while the BST predicts an area of 0.098 km^2.

Figure 10. Estimation of snow extent (m^2, red points) using the Blue Snow Threshold algorithm (BST) and measured snow depth from the SNOTEL stations (mm, blue points). Purple points indicate measurements of zero for both parameters. **(a)** The Quemazon, NM Snotel station (708) near Valles Caldera, NM, **(b)** the Truckee #2 Snotel station (834) near Truckee, CA **(c)** the Mt Ryan Snotel station (948) near Fairbanks, AK, and **(d)** the Bettles Field Snotel station (1182) in the southern Brooks Range, AK. The areal snow extent estimates were calculated by summing the number of pixels classified as snow within a 20 m radius of the Snotel station.